Università degli Studi di Napoli

"Federico II"

Department of Physics

PhD Thesis in

Novel Technologies for Materials, Sensors and Imaging

Nanowire Dimer Metamaterial For Sensing:

Design, Fabrication and Optical Characterization

Ndubuisi Emmanuel Jude Omaghali

Advisors:

Prof. G. Abbate

Prof. A. Andreone

Dr. V. Tkachenko

April 2013

To my Parents

Abstract

In this work a thorough study of the electromagnetic resonances excited in a planar metamaterial consisting of pairs of gold bars(dimers) arrayed on a dielectric substrate is reported. In the case of equal bar lengths, bright resonance mode can easily be excited, which couple strongly to free space and posses a low Q-factor. The introduction of bar length asymmetry induces the excitation of the so-called dark mode which couple very weakly to free space and show high Q-factors. The interaction of the dark and bright resonant modes results in a Fano type profile of the resonance. With increasing length asymmetry, coupling of the dark mode to free space is increased, resulting in a lowered Q-factor. The dependence of both the dark and bright modes on the dimer geometry and refractive index of the metamaterial environment is studied in order to optimize the structure for a potential application as an optical bio or chemical sensor. Effective material parameters are obtained from spectroscopic ellipsometry measurements of the metamaterial deposited on a glass substrate and their physical meaning and applicability are discussed. Experimental results show good agreement with simulation.

Acknowledgements

I thank God Almighty for His Mercy.

I thank my supervisors Prof. Giancarlo Abbate, Prof. Antonello Andreone and Dr. Vladimir Tkachenko for their wonderful supervision and guidance. For all the discussions, advice and contributions to the work, I sincerely say a very big thank you. The optical characterization would not have been possible without the help of Dr. Vladimir Tkachenko. I am grateful for their invaluable assistance in the course of my study and contributions to the work. Lots of thanks to Dr. Salvatore Savo, Boston College, USA, for his contributions and help with the fabrication.

Special thanks to Guido Celentano, to all my friends and everyone who has been a part of this in one way or another.

I thank my parents and family for their support.

Contents

List of Figures

List of Tables

CHAPTER 1

Introduction

1.1 Background

Metamaterials are a type of artificial materials which show properties that are usually not found in naturally occurring materials. Artificially designed and fabricated structures can be arranged to control electromagnetic wave through such material, thereby realizing novel electromagnetic effects[1].

Some of the exotic optical properties of such materials include negative refractive index, cloaking, electromagnetically induced, transparency(EIT), slow light and superlensing. Usually, the unit size of the particles of the metamaterial are much smaller than the wavelength of interest. Also, the interactions between the meta-atoms of the metamaterial can be controlled due to the flexibility in the geometry and size of the particles, thereby opening up many interesting areas of research and applications for such artificial materials. The size p or the unit cell of the "meta-atom" in a metamaterial is usually smaller than the driving wavelength of light $\lambda (p \ll \lambda)$.

Victor Veselago first reported materials with the electric field E, magnetic field, and wave vector κ, all forming a left handed system in his paper entitled "The Electrodynamics of Substances with Simultaneously Negative Values of ϵ and μ" in 1967[2]. In such a system, materials with both negative permeability and permittivity were shown

to be theoretically possible and named negative index materials(NIM). The lack of natural materials possieing these unique properties made experimental demonstration of NIM virtually impossible. However, practical demonstration of NIM was not shown until a hallmark experiment by Smith et al[3]. A medium composed of copper split ring resonators and continuous wires were shown to exhibit negative values of ϵ and μ in the microwave region. The structure is considered as an LC-circuit, with the rings forming the inductances and the gaps between the rings form the capacitors. For a magnetic field whose orientation is perpendicular to the plane of the split rings, an opposing magnetic field is induced and a frequency region of negative permeability can result. A combination of the split ring resonator providing the negative μ and the continuous wires providing the negative ϵ, led to a frequency region with both μ and ϵ simultaneously negative. Other demonstrations of metamaterials exhibiting negative index at microwave frequency have also been realized[4, 5]. Also of importance is the work of Pendry, in which he described the perfect lens for a NIM[6]. In conventional lenses, light can not be focused beyond the diffraction limit. However, Pendry showed that using a slab of negative refractive index material with $\epsilon = -1$ and $\mu = -1$, evanescent waves can be recovered, thus overcoming this limitation in conventional lenses. In the GHz frequency range, a negative index of refraction was experimentally demonstrated using a left handed material(LHM) composed of square copper split ring resonators and copper wires strips on opposite sides of a fibre glass circuit board by Shelby et. al in 2001[7]. The scattering angle of the transmitted beam through a prism is measured, with negative refraction angles as predicted by theory for a negative index material. Attempts have been made to realize optical metamaterials.

At optical frequencies, most materials are non magnetic with a permeability $\mu \approx 1$, a positive refractive index and a positive dielectric permittivity. Thus, by scaling down

the geometry and size dimensions of the meta-atoms, some of these exotic properties of metamaterial can be realised at optical frequencies. With the advancement of fabrication technology, the scaling of metamaterials to optical frequencies was made possible, hence the realization of these novel electromagnetic properties at optical frequencies. In particular, it has been shown that by scaling down the dimensions of the split ring resonator, negative magnetic permeability can be achieved in the terahertz frequency range[8]. However, for frequencies in the near-infra red and visible ranges, it not always possible to scale down. Contributing to this are the limitations in fabrication of structures with nanometer dimensions. Another limiting factor is the saturation of resonance amplitude with decreasing size due to increasing losses in the metals[9, 10].

In metallic nanoparticles, coupling between them nanoparticles can support collective electronic oscillations or surface plasmons. These interactions result in some phenomena such as Fano resonances[11], and electromagnetically induced transparency(EIT)[12], which have been demonstrated in meta molecules and still finding increasing research interest. In metamaterials, an arrangement of the sizes and dimensions of the nanostructures can lead to a control of these resonance interactions, thereby opening up possibilities for practical applications.

1.2 Motivation

In this dissertation I have investigated the resonant modes in nanowire metamaterial dimer, from design, fabrication, optical characterization using spectroscopic ellipsometry technique, and I studied possible applications of the device. The objectives were to design a nano structured device for sensing, with operating frequency in the optical regime. I demonstrate that the asymmetric dimer configuration of nanowires supports

a strong Fano-type resonance, from interference between dark and bright resonances. Experimental measurements show a good agreement with the numerical simulations. At optical frequencies the behaviour of metals comprising the nanowires are very lossy and can no longer be assumed to follow the standard Drude model. Obtaining low loss and high quality factor is of interest at optical frequencies for applications in areas such as sensing and tunable optical devices. In this thesis I also explored the possibility of using the nanowire dimer for biological and chemical applications. Given the very small dimensions and sizes of the nanostructures, fabrication of the device becomes more stringent. Hence, another objective was to develop a fabrication process with good repeatability for the fabrication of the nanostructures. A further objective was the detailed investigation of the optical response of the structure using spectroscopic ellipsometry techniques. The ellipsometer as an instrument is quite sensitive as it not only measures the intensities of light but also gives the ratio of the phase changes between the polarizations. However, its use in metamaterial characterization is not widespread and moreover is heavily debated in literature. Thus, in this dissertation I also explored the feasibility of the optical characterization of the fabricated sample using ellipsometric techniques.

1.3 Thesis structure

In this dissertation, a thorough study of nanowire dimers and properties of the resonances of the structure for the optical frequency regime is presented. Characterization using the methods of spectroscopic ellipsometer is discussed.

In Chapter 2, the design of the nanowire dimer. The excitation of bright and dark mode resonances in the structure has been investigated using Finite-Difference Time-

Domain(FDTD) simulations. In the symmetric dimer configuration with equal lengths of nanowires, only a bright mode resonance is present. However, with the introduction of a length asymmetry within the structure, the dark modes can be excited. The behavior of the resonances is described using a hybridization model for the dimer. The Fano-type resonance of the dark mode with a characteristic quality factor higher than that for the bright mode is exploited for possible applications as a sensor due to its high sensitivity and figure of merit(FOM). The possibility of a tunable device using the dimer is discussed.

Chapter 3 reports the fabrication procedure for the dimer nanostructures described in Chapter 2.

In Chapter 4 the optical characterization of the fabricated nanostructure using spectroscopic ellipsometry techniques is discussed. A description of the procedure involved is outlined. Optical models were obtained from the matching of the measured ellipsometer parameters Ψ and Δ to those simulated by fitting to a model of structure. From the fit, the dielectric properties of the substrate and the fabricated nanostructures is extracted. Experimental measurements are shown to be in agreement with numerical results that were discussed in Chapter 2.

Chapter 5 discusses the possible applications of the dimer metamaterial as sensors for biological or chemical sensing. Here, we have shown that the dark modes are generally sensitive to changes in the dielectric environment compared to the bright, due to the higher quality factor resulting from a higher electromagnetic energy confinement. This property of the dark modes has been employed towards realizing a possible sensing device, with a Figure of Merit as high as 7. Also, the possibility of a tunable device has been investigated, with the resonances being controlled by an anisotropic environment,

with the dimer showing a high promise as a tunable device. Finally, we have discussed the possible challenges and future extension to the work discussed so far.

CHAPTER 2

Metamaterial Dimer Design

2.1 Introduction

Recently, the tremendous advances in material science and technology have led to the implementation of new classes of artificial electromagnetic materials called metamaterials, that can be define as composites with useful and unusual electromagnetic properties offered by the specific response of constituents. In anomalous effects such as negative refraction[13, 14], optical magnetism[15], optical activity without chirality of scatterers[16] etc., the geometrical shape of "metamolecules" plays a decisive role. Most of these properties originates from the ability of scattering elements to support resonances. The flexibility in the geometry of metamaterials has enabled the tailoring of interactions between resonances. In symmetric "metamolecules", super radiant or bright modes couple to the incident field, producing broad and lossy resonances. With the introduction of asymmetry in the geometry, trapped or dark modes which are not normally excited in the symmetric structure can be excited[17, 18]. These dark mode resonances weakly couple to free space[19] and therefore have high quality factor Q. A Fano type resonance can result from the interference of the bright and dark modes, resulting in an asymmetric spectral profile[11]. Studies of this resonance in various plasmonic systems have been carried out over the years[20]. Fano resonances caused

by symmetry breaking have been reported in different structures such as vertically stacked metal nanowire pairs of same length and displaced along their axis[21], split rings[22], ring/disk systems[23, 24], just to list a few. These induced resonances have the ability to concentrate the electromagnetic field in small regions thereby increasing the interaction with matter, thus making them suitable for applications such as sensors[25–29]. Increasing the Q factor of dark modes is particularly important for planar metamaterials (nanostructured metasurfaces) which are optically thin structures and therefore don't have a resonating volume for high energy confinement. Planar metamaterials with engineered surface plasmon polaritons are promising for application as chemical and biological sensors. Thus, the size and shapes of these nanoparticle greatly affect the resonances, which is also known to be affected by the dielectric environment around the nanoparticles[30]. For near infrared or visible wave ranges, the sizes and dimensions of the planar nanostructures necessitate the need for advanced fabrication mechanism, which in most cases can be quite expensive, depending on the complexity of the structure. Therefore, a reduction in the complexity of their geometry is highly desirable, since this would decrease fabrication time and cost dramatically.

We numerically study a planar metamaterial composed of gold nanorod dimers and the excitation of dark Fano type resonances in this structure. We report on the parametric analysis of the modes excited by electromagnetic wave incident onto the metasurface. The calculated transmission spectra are explained using distributions of local electric field and current on the nanorod surface. The Fano resonance, which is excited due to the asymmetry in the length of the nanorods of the dimer, shows a high quality factor and a sharp dependence of its frequency on the ambient environment refractive index. These properties of the dimer are discussed in view of the possible application of the asymmetric dimer metamaterial for optical sensing.

2.2 Dimer metamaterial geometry and numerical model

The periodic arrangement of metallic dimers can mimic magnetic atoms, which have been shown in structures such as split ring resonators, etc. In the dimer configuration, the arrangement of the nanowires is such that coupling between the nanowires can result in resonances which display different responses to the incident electric field. The observed resonance behavior resulting from the coupling can have peculiar properties related to the manner in which the coupling occurs. Hence, depending on the coupling, symmetric and asymmetric resonance behaviors can be excited in the structure. The dimer metamaterial(metasurface) structure studied here is composed of gold nanorods of varying length deposited on an Indium Tin Oxide(ITO) coated glass substrate. The very thin(25nm) ITO film acts as an adhesive layer. The unit cell of the dimer structure is sketched in Fig. 2.1 whereas in Fig. 2.2, a three dimensional view of the structure is shown.

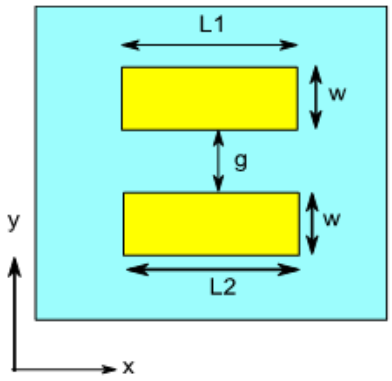

Figure 2.1: Schematic of the dimer metamaterial unit cell. The geometrical parameters of the dimer are the lengths $L1$ and $L2$ of the gold nanorod(yellow). The nanorods have equal widths of $w = 70nm$ are separated by a gap size of $g = 50nm$. The gold thickness is $30nm$ for both nanorods.

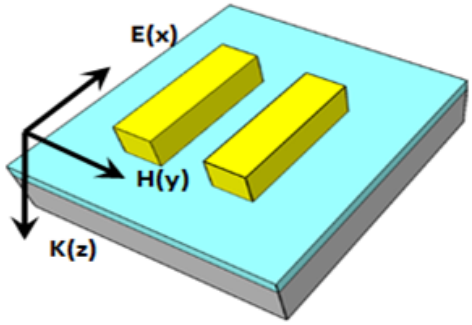

Figure 2.2: Incident field is along the z direction, normal to the plane of the dimer, with electric field polarization E along x direction. The periodicity of the structure is $300nm$ along both the x and y directions.

The lengths of the gold nanowires(yellow) are $L1$ and $L2$. The value of $L2$ is fixed at $200nm$, whereas $L1$ is varied. Both nanowires have equal width $w = 70nm$ and thickness(along z-direction) of $30nm$. The nanowires are separated by a gap of $g = 50nm$. The dimers are distributed periodically in the x and y directions with a periodicity of $300nm$ in both directions. The permittivity of the ITO layer and the glass substrate are taken as 3.8 and 2.25 respectively. To model the gold response, a Drude model for the dielectric function $\varepsilon(\omega)$, given by $\varepsilon(\omega) = 1 - \frac{\omega_p^2}{\omega^2 + i\gamma\omega}$ is used, where ω_p is the plasma frequency, γ the damping constant and ω the frequency. A plasma frequency of $1.37 \times 10^{16} Hz$ is used. A damping rate of $1.2 \times 10^{14} Hz$ was used, taking into account the scattering losses in the gold film[26, 31–33]. A finite difference time domain (FDTD) commercial solver, CST MWS, was employed to perform the numerical electromagnetic simulations for the structure. In the simulations, the incident wave propagation direction is along the z-axis, normal to the plane containing the gold nanowires, and is polarized along the x-axis as shown in Fig. 2.2. In this study of the metamaterial dimer, we define a length asymmetry $\alpha = L2 - L1$, that is the length difference between the gold nanowires.

2.2.1 Spectrum for single nanowire and dimer

The electromagnetic response of a single nanowire of the dimer can be firstly simulated. In this case it is the nanowire of length $L2$ on the ITO coated glass substrate. With the electromagnetic wave incident on the planar surface, as shown in Fig. 2.2, the spectrum of the scattering parameter S_{21}, corresponding to the transmission coefficient is shown in Fig. 2.3.

In this single nanowire configuration, a broad resonance at around $300THz$ is excited. This resonance is a dipolar type resonance, as seen from the electric field plot at resonance, shown in Fig. 2.4.

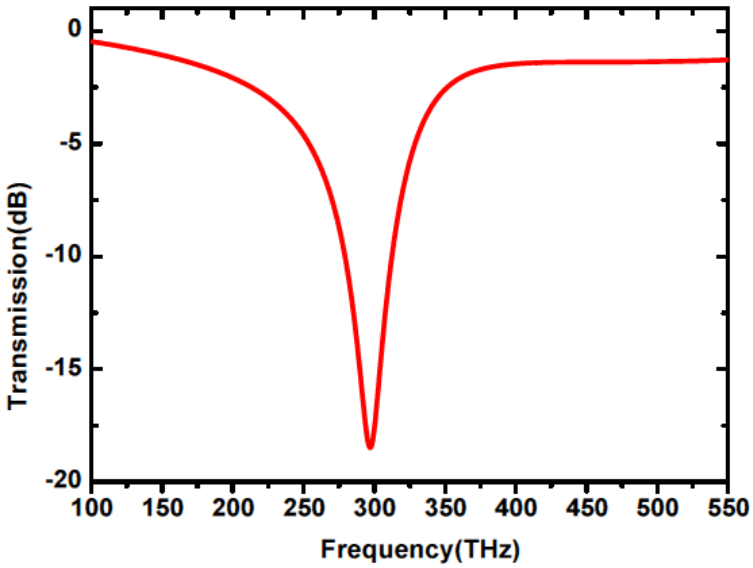

Figure 2.3: Transmission spectrum for a single nanowire of the dimer.

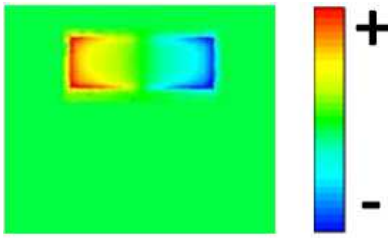

Figure 2.4: Electric field distribution at resonance in the nanowire.

Also, the current density at resonance further shows the charge oscillation at resonance

with a dipole like behaviour.

2.2.2 Symmetric and asymmetric dimer

A combination of the nanowires of length $L1$ and $L2$ is then investigated for different dimer configurations. In the symmetric dimer, with $L1 = L2$, the resonance of the structure is simulated again for an incident wave normal to the dimer surface and electric field polarization along the dimer long axis as shown in Fig. 2.2. In the symmetric dimer with $L1 = L2$ or $\alpha = 0$, a single resonance is excited at a frequency of around $340THz$ (see Fig. 2.5). This resonance is similar to the one shown by the single nanowire in Fig. 2.3. Thus, a combination of both nanowires in the dimer does not effectively change the nature of the resonance. The electric field distribution in the symmetric dimer at resonance is shown in Fig. 2.6. The symmetric dimer behaves as a dipole with a field distribution which is in phase in both arms of the dimer. The field distribution results in a current distribution in both arms of the dimer. From the current density plot, a parallel current oscillation in both arms of the dimer is observed as shown in Fig. 2.7. The field in both arms of the dimer interferes constructively, resulting in the radiant nature of the observed broad resonance. In the absence of length asymmetry or $\alpha 0$, a broad dipolar resonance therefore occurs at about $341.2THz$, which represents a bright or super radiant mode with a strong coupling to free space.

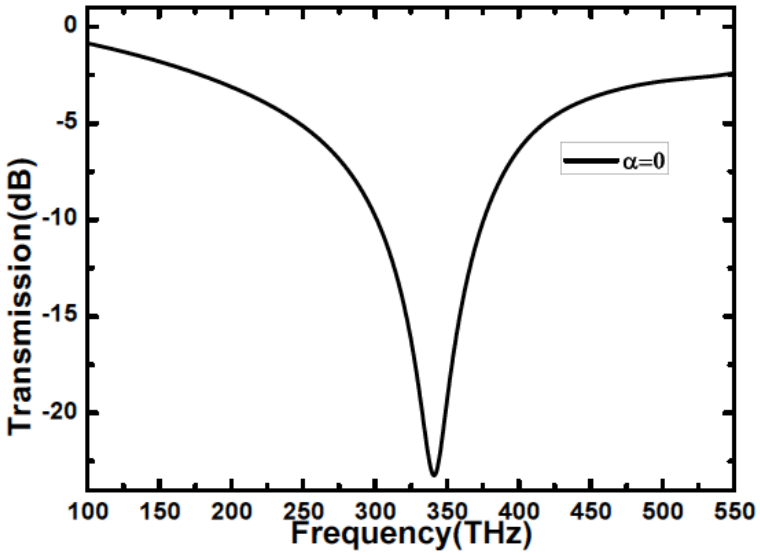

Figure 2.5: Transmission spectrum for the symmetric dimer($L1 = L2$).

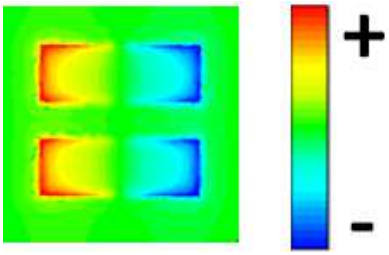

Figure 2.6: Electric field distribution in the symmetric dimer at resonance with $\alpha = 0$.

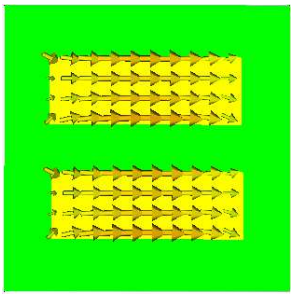

Figure 2.7: Current density in the symmetric dimer at resonance with $\alpha = 0$.

We then consider the dimer structure with a length asymmetry parameter $\alpha = L2 - L1$introduced in the length of the nanowires. In the study, $L2 = 200nm$ whereas $L1$ is varied to introduce the asymmetry. The asymmetry is introduced from both ends of $L1$(as shown in Fig. 2.8) such that a mirror plane still exists normally to the long axis of the nanowires.

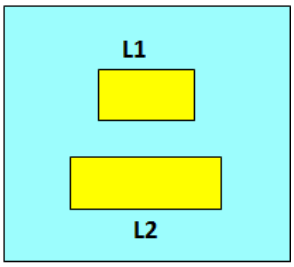

Figure 2.8: Asymmetric dimer configuration. The asymmetry is introduced with the length $L1$ of a single nanowire from both ends so that $\alpha = L2 - L1 \neq 0$.

For a dimer with lengths $L1 = 170nm$ and $L2 = 200nm$ or asymmetry length parameter of $\alpha = 30nm$, we simulate its resonance response to the external field due to the influence of the introduced asymmetry. With the introduction of asymmetry, we can observe two resonances: a higher frequency resonance at around $360THz$ and an associated lower frequency resonance at around $270THz$, as shown in the transmission spectrum in Fig. 2.9. The lower frequency resonance is very narrow compared to the broad higher frequency resonance.

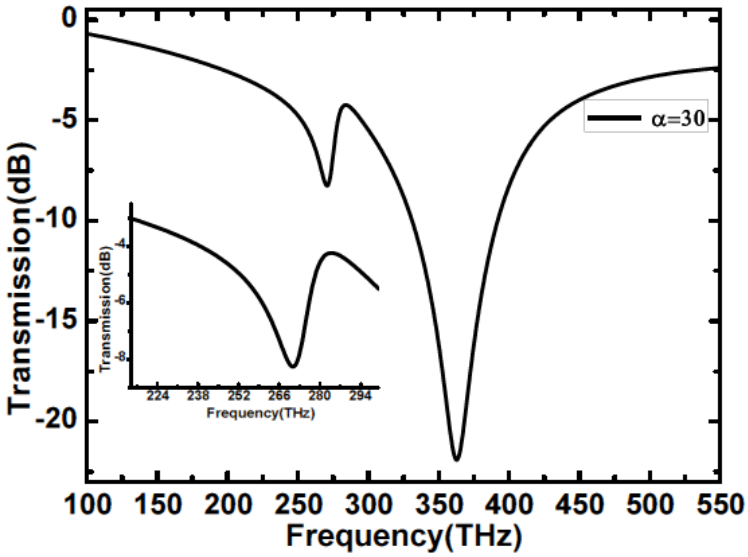

Figure 2.9: Transmission spectra for the Asymmetric dimer with $\alpha = 30nm$ and $L1 = 170nm$. Inset shows the excited dark resonance.

The characteristics of these excited resonances in the asymmetric dimer can be highlighted from their field distributions. Thus, we calculate the electric field distributions

at the respective resonances for the narrow lower frequency and the broad higher frequency respectively. For the higher resonance frequency around $360THz$, this is shown in Fig. 2.10

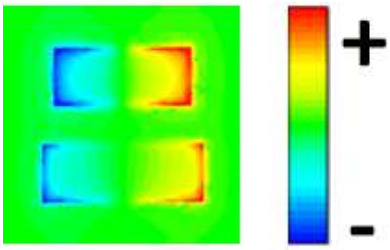

Figure 2.10: Electric field distribution in the asymmetric dimer with $\alpha = 30nm$ for the bright mode resonance. The electric field is in phase in both arms of the asymmetric dimer.

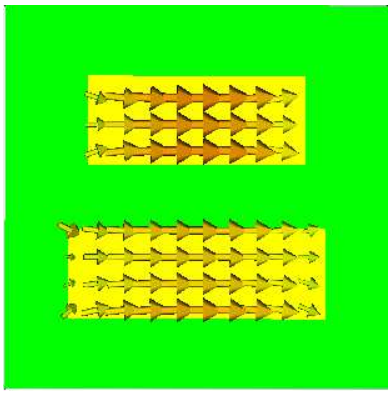

Figure 2.11: Current density in the asymmetric dimer with $\alpha = 30$ at the bright mode resonance.

At resonance, this higher mode displays a dipole-like oscillation. In both arms of the asymmetric dimer, the field distribution is in phase. This higher resonance is a bright mode with characteristics similar to the bright mode resonance in the symmetric dimer configuration. Likewise, the current distribution for this resonance is shown in Fig. 2.11. A parallel current oscillation in both arms of the asymmetric dimer $L1$ and $L2$ is induced at resonance for the bright mode, similarly to what happens for the bright mode resonance in the symmetric dimer(Fig. 2.7).

As shown in Fig. 2.9, in addition to the already higher frequency resonance bright mode which easily couples to the incident field, a lower frequency resonance mode is also

excited. In the symmetric dimer spectrum in Fig. 2.5, this lower resonance mode is not present. This subradiant or trapped mode shows a weak coupling to the incident beam [34], thereby displaying a narrow resonance profile compared to the bright mode. The nature of this dark mode can be further seen from the field distribution in the arms of the asymmetric dimer at resonance, in Fig. 2.12. An opposite field distribution can be observed in the dimer arms $L1$ and $L2$, with a π phase difference between the fields. This results in an antisymmetric current oscillation in both arms of the dimer at the dark mode resonance as shown in the current density plot in Fig. 2.13, explaining the very low radiation loss of this mode[19, 22, 35].

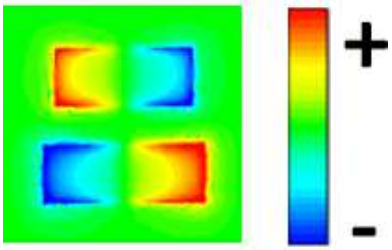

Figure 2.12: Electric field distribution in the Asymmetric dimer with $\alpha = 30nm$ for the dark mode resonance, with opposite field distribution in the dimer arms L1 and L2 respectively.

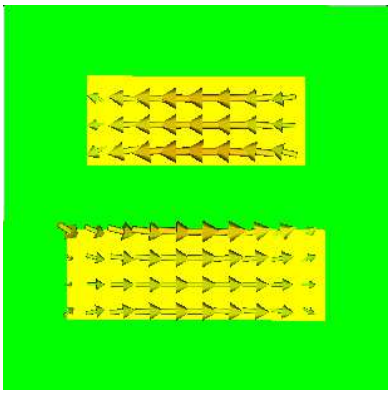

Figure 2.13: Current density in the asymmetric dimer with $\alpha = 30nm$ at the dark mode resonance.

The surface current distribution shown in Fig. 2.13 indicates that the lower energy resonance is of magnetic origin. The induced parallel(Fig. 2.11) and anti-parallel(Fig. 2.13) current behaviour for the bright mode and the dark mode respectively in the asym-

metric dimer can be attributed to the bonding and anti-bonding modes in plasmon resonance hybridization[36], as it will be explained in the next section.

Interference between the bright and the dark modes can occur, resulting in a Fano-type profile of the resonance as seen from the dark mode resonance in Fig. 2.9. The sharp asymmetric Fano-type profile of this resonance shows some characteristic dip and peak features[19, 21, 22, 29, 37, 38].

2.2.3 Plasmon Hybridization in the dimer

In this section the resonance behavior in the dimer metamaterial using a plasmon hybridization picture[36, 39] is described. The subradiant resonance of the asymmetric dimer can be viewed in terms of an LC circuit. The anti-parallel currents contribute to the inductance L, whereas the gap between the nanowires of the dimer contribute to the capacitance C. The interaction between the individual nano wires of the dimer gives the overall plasmon response of the dimer structure. Fig. 2.14 shows a picture of the hybridization scheme for the dimer. For the symmetric dimer, only a single resonance appears at energy level $\mid w_0 >$. With the introduction of asymmetry in the dimer, with $L1 \neq L2$, two resonances are excited. The plasmon hybridization in asymmetric dimer results in the excitation of two separate modes with a higher energy level $\mid w_+ >$ and a lower energy level $\mid w_- >$ as shown in the spectrum in Fig. 2.15. The higher energy level is the bright dipolar resonance whereas the lower energy level is the dark subradiant mode. At the higher energy mode $\mid w_+ >$, an in-phase charge oscillation results in a repulsive force between the nanowries $L1$ and $L2$ of the asymmetric dimer. This is synonymous to the anti-bonding response. Whereas, at the lower energy mode $\mid w_- >$, the anti-phase charge distribution results in an attractive force between the nanowires of the dimer, resulting therefore in a bonding response between

the nonowries $L1$ and $L2$ of the dimer. The near field mode splitting is induced because of the plasmon hybridization[17]. The near-field interaction is repulsive(attractive)for the bright(dark) mode resonances, hence the energies are higher(lower), as depicted in Fig. 2.14.

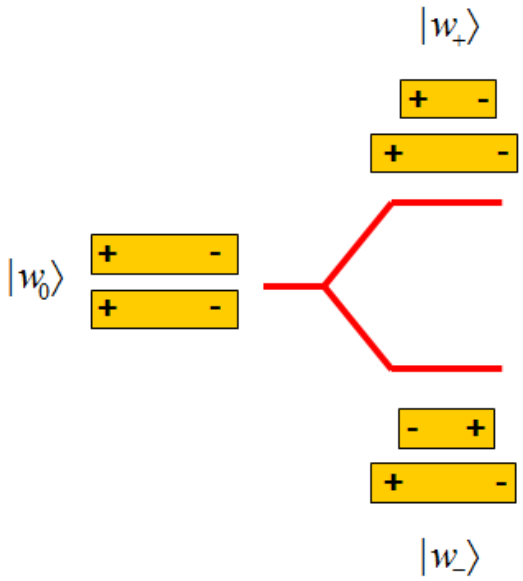

Figure 2.14: Hybridization scheme for the dimer. In the symmetric configuration, only a single mode resonance at energy level $\mid w_0 >$ is present. In the asymmetric dimer, with $L1 \neq L2$, a degeneration of energy levels with a higher energy $\mid w_+ >$ and a lower $\mid w_- >$ occurs.

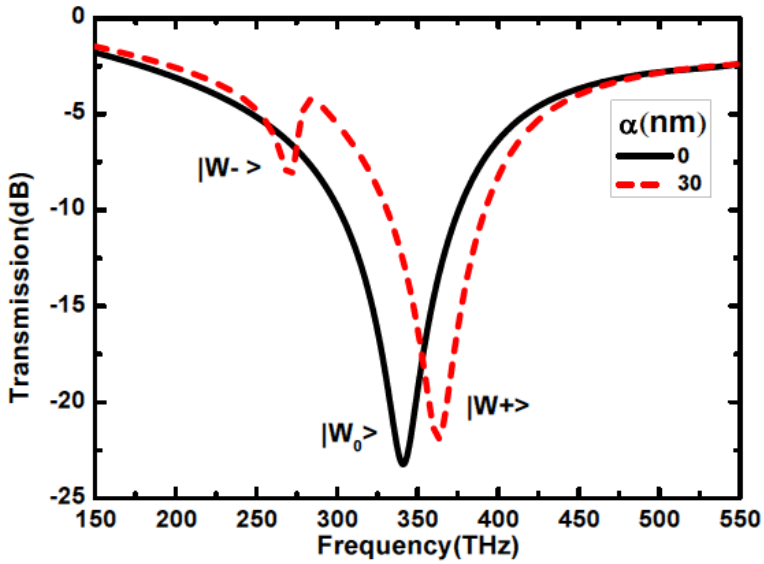

Figure 2.15: Transmission spectrum of the dimer. The even black curve shows the spectrum for the symmetric dimer with dimer lengths $L1 = L2 = 200nm$. The symmetric dimer shows a resonance at $\mid w_0 >$. Whereas for the asymmetric dimer with length asymmetry parameter $\alpha = 30nm$ two resonances $\mid w_- >$ and $\mid w_+ >$ at lower and symmetry higher energies are excited.

2.2.4 Geometrical tunability of the dimer

The degree to which asymmetry affects the dark and bright mode is discussed in this section. We calculate the dependence of the bright and dark resonance modes on the asymmetry parameter α is studied. The resonance response for various values of α have been calculated. With increasing values of α from 10 to $40nm$, its effect on the bright and dark modes is shown in Fig. 2.16.

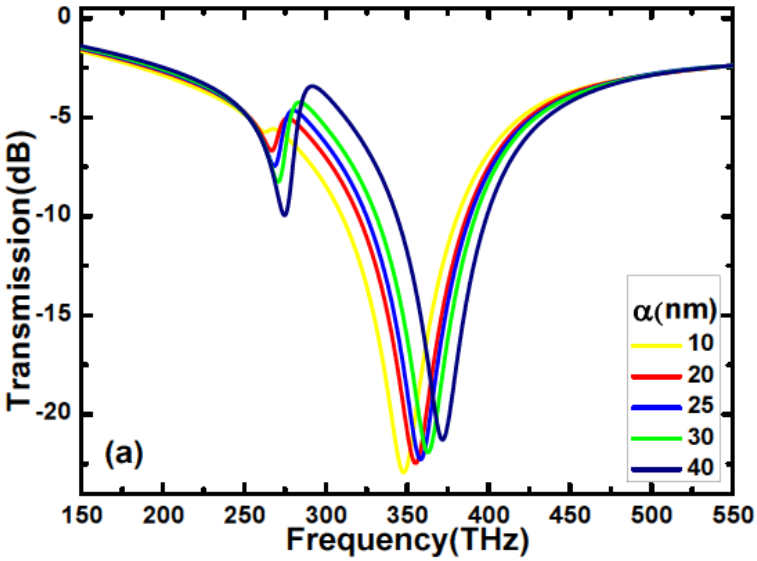

Figure 2.16: Bright and dark mode resonances as α is increased from 10 to 40nm.

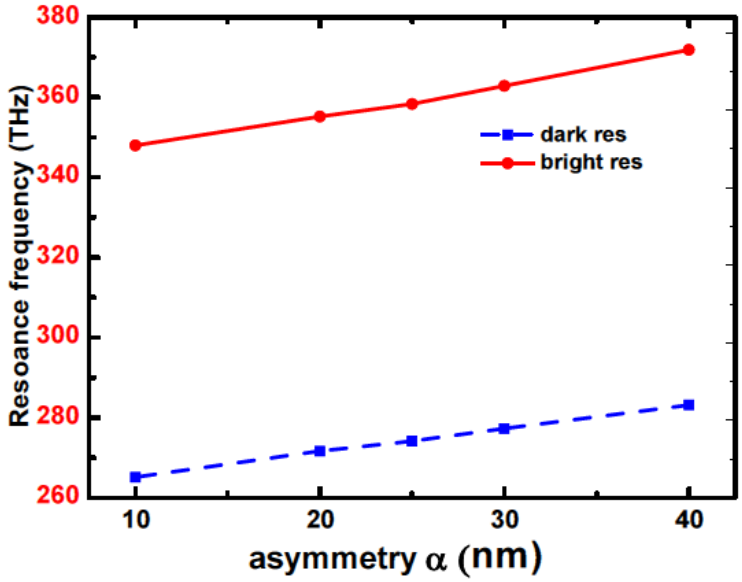

Figure 2.17: Bright and dark mode frequencies for different values of length asymmetry α ranging from 10 to 40nm. With increasing α, both bright and dark modes are blueshifted.

From Fig. 2.16, with increasing length asymmetry, there is an increase in both the bright and dark mode resonance to higher frequencies. The resonance frequency has an inverse dependence on the length of the dimer, and thus the observed blue shifts plotted in Fig. 2.17. Then there is a broadening of both dark and bright modes respectively, as also shown in Fig. 2.16. With increasing asymmetry, the modes show a higher cou-

pling to free-space and consequently higher energy losses, resulting a lowering of the Q factor value for both modes. However, on a careful examination, it can be observed that the modes do not broaden at the same rate for a given value of length asymmetry. The dark mode(Fig. 2.18), shows a greater degree of broadening compared to the bright mode for each length asymmetry. Its behaviour is due to the higher coupling of light to incident radiation than in the bright mode, as length asymmetry is increased. Of course, a red shift is observed for negative values of asymmetry($L1 > L2$).

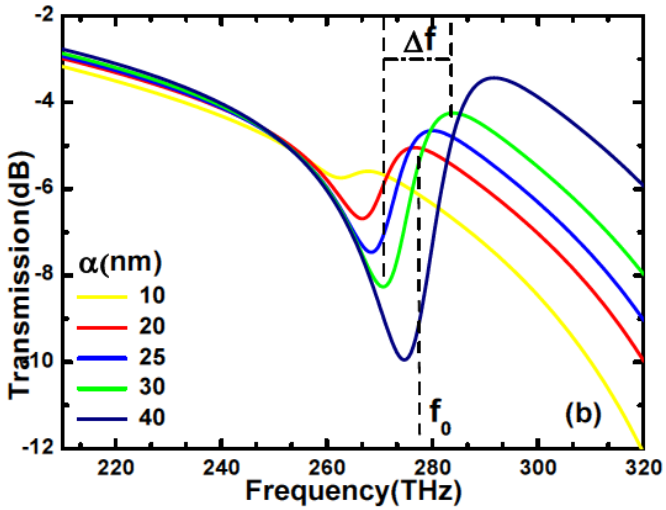

Figure 2.18: Dark mode dependence on asymmetry. $\triangle f$ and f_0 shown for the length asymmetry 30 nm.

This property of the dark mode is of importance for various applications due to its responsiveness to perturbation, thus making it possible to build various optical sensing devices. This will be discussed in Chapter 5.

So far, we have discussed the asymmetric dimer in which asymmetry is symmetrically from both ends of the nanowire $L1$ as depicted in Fig. 2.8. However, length asymmetry in the nanowire $L1$ from one end only can be introduced, for the same length asymmetry parameter α, as depicted in Fig. 2.19.

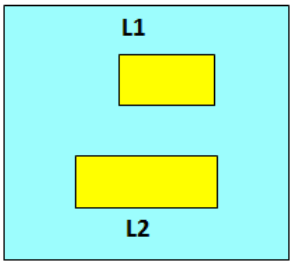

Figure 2.19: Asymmetric dimer configuration. Here the asymmetry is introduced from one end only of the nanowire $L1$.

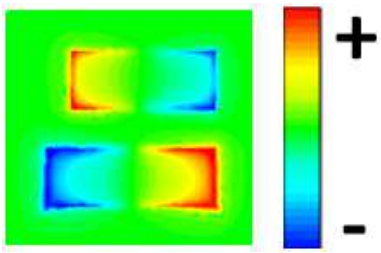

Figure 2.20: Electric field distribution at the dark mode resonance in the asymmetric dimer depicted in Fig. 2.19 with $\alpha = 30nm$.

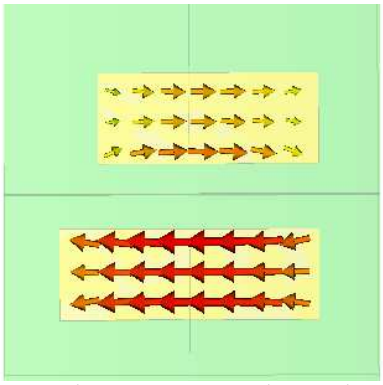

Figure 2.21: Current density in the asymmetric dimer depicted in Fig. 2.19 with $\alpha = 30nm$ at the dark mode resonance. Anti-parallel current oscillation is induced in both arms of the dimer.

Once again, Fig. 2.20 shows an anti-phase field distribution in the dimer at the dark mode resonance. Thus, an antisymmetric current oscillation in both arms of the dimer at the dark mode resonance is shown in current density plot of Fig. 2.21, similar to the asymmetric configuration depicted in Fig. 2.8.

Likewise, for the bright mode, the field plots simulations in this asymmetric configuration show an in-phase field distribution as shown in Fig. 2.22 and the corresponding

current density distribution in both arms of the dimer in Fig. 2.23 respectively.

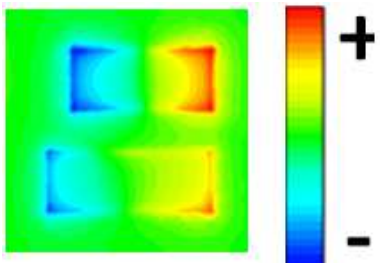

Figure 2.22: In-phase electric field distribution at the bright mode resonance with asymmetric dimer depicted in Fig. 2.19 with $\alpha = 30nm$.

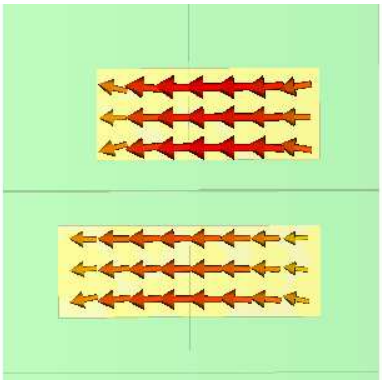

Figure 2.23: Current density in the asymmetric dimer depicted in Fig. 2.19 with $\alpha = 30nm$ at the bright mode resonance. Parallel current oscillation is induced in both arms of the dimer.

Irrespectively of the way in which the length asymmetry is introduced, similar resonances can be excited in the dimer for the same parameter α. Therefore, the difference in the dimer arms length appears to be the dominant factor responsible for the excitation of the dark modes.

2.2.5 Loss and quality factor of the resonances

In Fig. 2.24, the effect losses play on the nature of the resonance is shown. Attenuation in the metal can be considerably larger than the expected theoretical value using Drude model, since minimum size is comparable with the mean free path and because of this the complex fabrication techniques introducing additional losses in the structure. With increasing loss, there is a significant change in the amplitude of the resonances. Curves

show the spectral response for the asymmetric dimer with $\alpha = 30nm$ starting from the theoretical value of the collision frequency in gold, $w_c = 0.4 \times 10^{14}$.

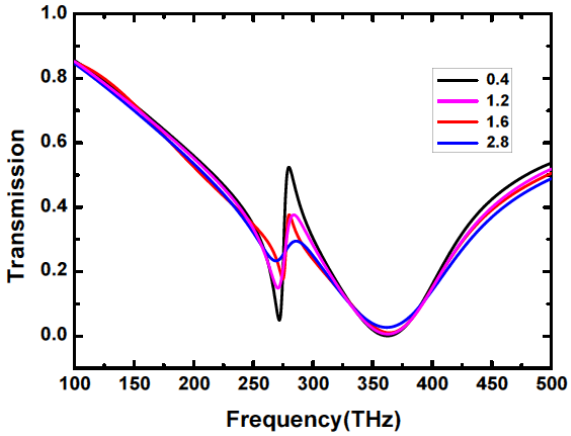

Figure 2.24: Spectral response for $\alpha = 30nm$ for losses in the gold. The resonances are strongly affected by the losses with a decrease in amplitude for different values of collision frequency $0.4, 1.2, 1.6, 2.1 \times 10^{14}$.

In section 2.2.4 we have discussed the effect of asymmetry on the nature of the dark and bright resonances, with both resonances broadening and blue shifting with increasing asymmetry. Of particular importance here is the broadening of the resonances. We discuss the effect of these broadening on the modes. As observed in section 2.2.4, the dark modes appear to broaden at a larger rate than the bright mode for the same length asymmetry α. This differing behaviour of the modes has some significant influence on certain properties of the resonance, in particular the quality factor(Q-factor) of the resonance.

The quality factor is usually defined as the ratio between the centre frequency and the full width at half maximum(FWHM) of the resonance(Lorentzian curve). For the Fano-type resonance of the dark mode the quality factor is defined as the ratio of the average frequency f_0 and the full width Δf between the peak and the antipeak (dip) at resonance[23](see Fig. 2.9). Obtaining high Q-factors in metamaterial resonators is highly desirable for sensing applications, since this implies a higher confinement of the

electromagnetic energy[18, 40].

From the resonant behavior of the dark and bright modes(Fig. 2.9), the respective Q-factors can be calculated for the corresponding asymmetry α, as presented in Fig. 2.25. For $\alpha = 10nm$, the Q-factor for the dark mode is 49 while the corresponding value for the bright mode is larger than 2. With increasing α up to $40nm$, a significant decrease in the Q-factor at the dark resonance is observed, whereas in the bright mode the resonance shows very little variation with α. From Fig. 2.25, the Q factor for the dark mode(black curve) is generally higher than that of the bright mode(red curve) for all values of length asymmetry, due to a higher concentration of electromagnetic energy. With increasing length asymmetry, the dark mode couples much stronger with free space, with a faster broadening of the resonances and a corresponding lower Q factor.

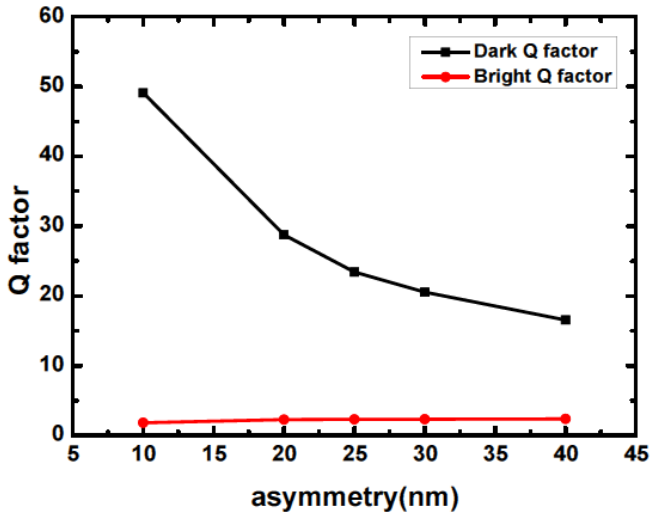

Figure 2.25: Influence of length asymmetry on the dark resonance (black line) and bright resonance(red curves) quality factors. With increasing length asymmetry, the dark modes shows a higher decrease in its Q-factors.

2.2.6 Absorption in the Dimer Structure

We can look at the behavior of the dark and bright mode resonances from their absorption spectra. The absorption is given by $A = 1 - R - T$, where R is the reflectance and T is the transmittance. For a dimer with $\alpha = 20nm$, the calculated absorption is

shown in Fig. 2.26. The absorption spectra for the dimer reveals a maximum at the positions of the transmission peaks, corresponding to the dark/trapped mode regions. At the respective bright and dark mode resonances, an absorption peak is observed to occur, with dark mode showing a higher absorption than the corresponding bright mode resonance peak.

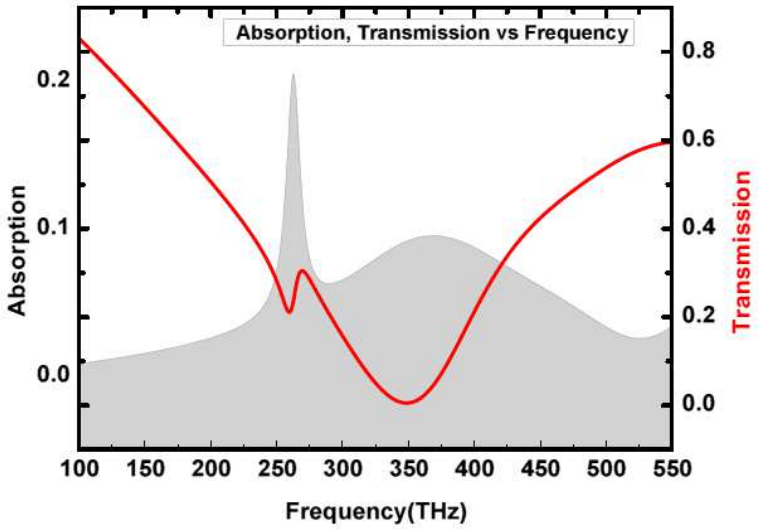

Figure 2.26: Absorption and transmission spectra for $\alpha = 20nm$

CHAPTER 3

Dimer Fabrication

The size of the dimer structures(which are of the order of nanometers) necessitates the use of an appropriate technology for its fabrication. Current patterning methods employed for nanofabrication include electron beam, nanoimprint, sidewall transfer, molecular beam epitaxy and other top-down fabrication methods, each one having its own advantages and disadvantages. For the fabrication of our structure, we are employing the electron beam lithography(EBL). The samples have been fabricated at Boston College, USA.

Two different substrates have been used for the fabrication of the dimer, namely a silicon substrate and an ITO coated glass substrate. We describe the basic procedures involved in the fabrication process of the dimer, with a schematics of the basic fabrication procedure shown in Fig. 3.1.

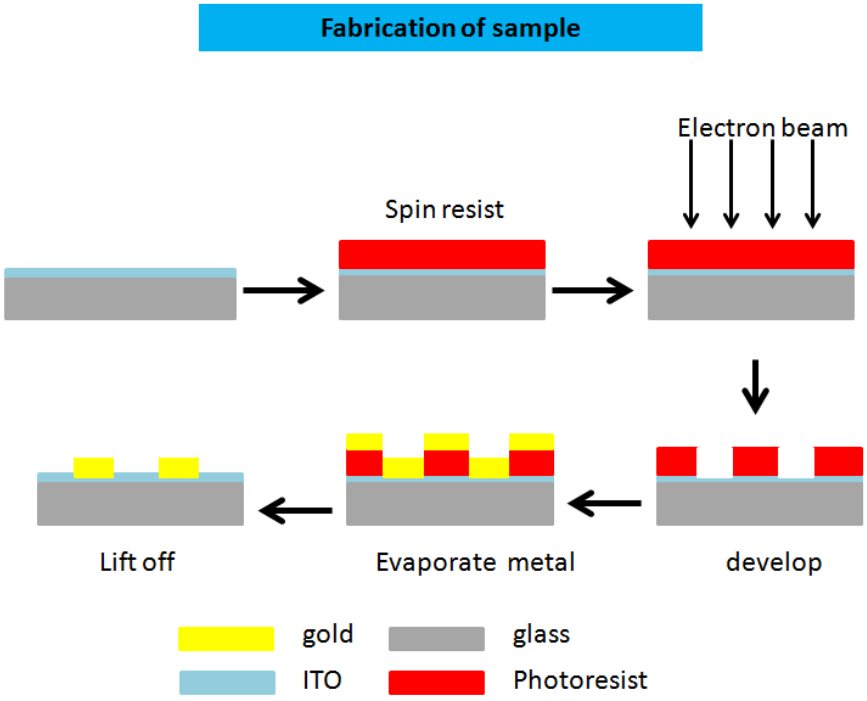

Figure 3.1: Fabrication procedure for the dimer. The photoresist(red) is spun on the substrate(grey) and a beam writing is realized. Following this is the development, and then the deposition of the gold(yellow), after which a lift of procedure is carried out.

1. Substrate Preparation

   - The substrate is cleaned using acetone an then dried with a Nitrogen gun before the photoresist is spun.

2. Spin coating

   - PMMA (polymethyl methacrylate) 495$A8$ is spin coated on the substrate. The resist contains 50% of $A8$ and 50% of photoresist thinner. It was spin coated at 3500rpm for 45 seconds, after which it was soft baked on hot plate at 180 $^\circ$ for 90 seconds.

   - Next, a layer of PMMA (polymethyl methacrylate) 950$A9$, which is 25% $A9$ and 75% photoresist thinner is spun at 3500rpm for 45 seconds. Following this, sample is then softbaked at 180 $^\circ$ for 90 seconds.

3. Electron beam lithography

   - The pattern of the dimer is written into the photoresist layer using the electron beam lithography(JEOL JSM-7001F). The exposure dose is $500 mJ/cm^2$.

4. Development

   - After the beam writing, the next step in the fabrication process is the development. This involves dissolving the photolysis a suitable developer solution depending on weather it is a positive or a negative photoresist. The PMMA photoresist used is a positive type photoresist. Thus, the molecular chains of the PMMA bonds are broken down during exposure to the electron beam writing process, making the exposed areas of the PMMA layer soluble in specific positive photoresist developers. The developer used is Methyl isobutyl ketonebonds(MIBK). The sample is placed in MIBK for 5 minutes, after which it is rinsed in Isopropyl alcohol(IPA) for 3 seconds. Then it is rinsed in water and dried.

5. Metal deposition

   - After the development, the next step in the process is the deposition of the metal layer. The evaporation process was done under vacuum using the Sharon Vacuum. First, $5nm$ Titanium(Ti) layer is deposited. This Titanium layer acts as an adhesive layer for the gold metal.
   - After the deposition of the Ti adhesion layer, a $30nm$ layer of gold metal is evaporated onto the sample.

6. Lift off

- After the gold deposition, a lift off procedure is performed. During the lift off, a suitable solvent is used to completely etch the deposited PMMA photoresist as shown in Fig. 3.1. For this procedure, a Microposit remover 1165 is used. The Microposit remover 1165 is a positive resist etchant for the positive PMMA resist. The wafer is put in a tank of Microposit remover 1165 and allowed to soak for 12 hours. After this, the wafer is removed and then rinsed with isopropanol and water. The wafer is then dried with an air gun.

SEM images of the fabricated dimer on silicon and glass substrates are shown in Fig. 3.2 and Fig. 3.3 respectively.

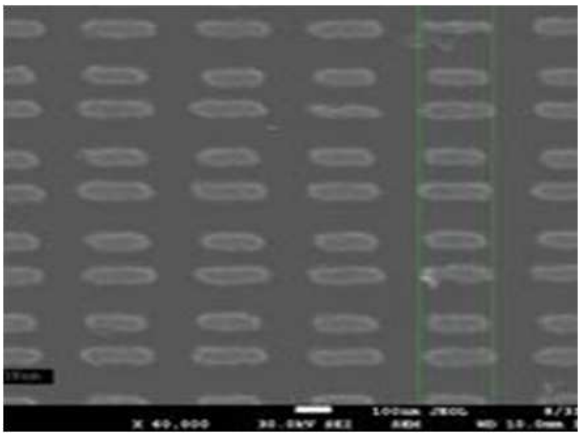

Figure 3.2: SEM image of fabricated dimer on silicon.

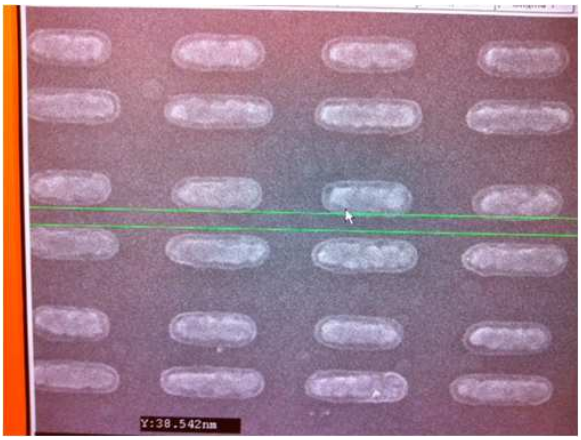

Figure 3.3: SEM image of fabricated dimer on glass.

In the next chapter/sections we describe the optical characterization of the fabricated

device using spectroscopic ellipsometry.

CHAPTER 4

Spectroscopic Ellipsometry Characterization of Metamaterial Dimer

4.1 Introduction

In this chapter we use the spectroscopic ellipsometric method to experimentally characterize the dimer metamaterial structure. The optical constants of the gold thin film on glass and silicon substrates are measured as well. We also discuss the procedure and highlight the advantages and disadvantages of using this procedure compared to other spectroscopic techniques.

4.2 A short introduction to Ellipsometry

The collective resonant response of the electrons in the nanowires of the dimer leads to high energy concentration, making them very sensitive to alterations in the dielectric environment and size of nanostructures, which can be observed from the resonance frequency positions, amplitude and absorption curves. With spectroscopic ellipsometry, measurement of polarized light reflected from the surface of a material can be performed and from these measurements the optical properties can be determined[41, 42]. However, the ellipsometric measurements were initially applied to macroscopic struc-

tures such as thin films, isotropic and homogenous media due to the complicated modelling nature of the process. The whole modelling process was simplified with the introduction of computers, thereby leading to a great advancement in ellipsometry measurements, and consequently its application to nano structures. When light is incident on a material, the electric and magnetic field of the light undergoes changes after reflection or transmission through the material, resulting in charge displacements. The resulting charge redistribution and currents in the material is described by Maxwell's equations relating the dielectric functions to the external electric and magnetic fields to the fields inside the material. For the electric field, this is given by

$$\mathbf{D} \equiv \varepsilon\varepsilon_0\mathbf{E} = \varepsilon_0\mathbf{E} + \mathbf{P} \tag{4.2.1}$$

where $\mathbf{D}$ is the electric displacement, $\mathbf{E}$ is the electric field, $\mathbf{P}$ the electric polarization, ε_0 the permittivity of vacuum and ε is the relative permittivity. For the magnetic components we have

$$\mathbf{B} \equiv \mu\mu_0\mathbf{H} = \mu_0\mathbf{H} + \mathbf{M} \tag{4.2.2}$$

where B is the magnetic field, $\mathbf{H}$ the magnetic induction, $\mathbf{M}$ the magnetic polarization, μ_0 is the permeability of vacuum and μ the relative permeability. To determine these optical properties of materials, the reflectance and transmittance (R&T) and ellipsometry measurements are required, though for some opaque materials, obtaining a transmission measurement be a difficult task. Basically, polarization changes are induced for light reflected(transmitted) from the surface of a material. This change in the polarization of the light depends on the way the electric field is polarized with respect to the incidence plane. Fig. 4.1 shows the schematic of reflection of polarized light from

the surface of a material. The electric field components and normal to the plane of incidence, p and s-polarizations respectively, acquire a phase difference Δ after reflection from a surface, with differing field reflected amplitudes.

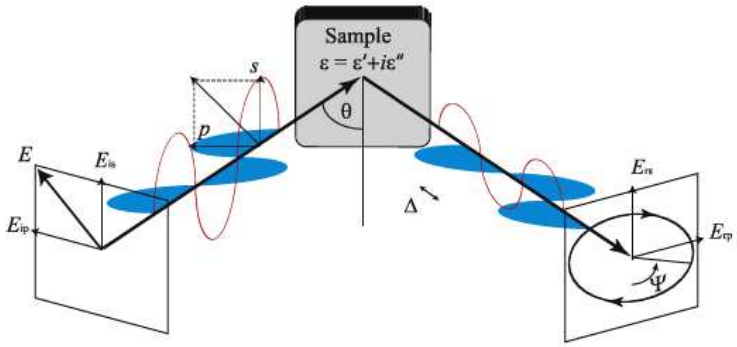

Figure 4.1: Ellipsometer measurement process

Provided the polarization of the incident light is known, then from the measured ellipticity of the state of the light after reflection, the optical constants of the material can be deduced. Depolarization can occur in certain samples with inhomogeneity in thickness, roughness, slight change in incident angle of the probe beam etc. In such situations, a Mueller matrix ellipsometry(MME) formalism is employed for the determination of the dielectric function. A Jones matrix can be used to describe the optical behavior for non-depolarizing samples, given by:

$$\begin{bmatrix} E_{rp} \\ E_{rs} \end{bmatrix} = \begin{bmatrix} r_{pp} & r_{ps} \\ r_{sp} & r_{ss} \end{bmatrix} \begin{bmatrix} E_{ip} \\ E_{is} \end{bmatrix} \tag{4.2.3}$$

where $E_{ip}\ (E_{rp})$ and $E_{is}\ (E_{rp})$ are the incident(reflected) p- and s- polarized component of electric field respectively. The matrix reflection coefficients are: r_{sp} for the reflected s polarized light induced by an p-incident light, r_{ps} for the reflected p polarized light induced by an s-incident light. The diagonal elements r_{pp} and r_{ss} are the well known Fresnel coefficients and are denoted as r_p and r_s respectively. Thus, in reflection mode,

we can obtain the ellipsometric parameters Ψ_r and Δ_r as

$$\rho_r = \frac{r_p}{r_s} = tan\Psi_r exp(i\Delta_r) \tag{4.2.4}$$

where ρ_r is the complex-valued ratio between the reflection coefficient for orthogonal polarizations.

Similarly, in transmission mode, the ellipsometric parameters Ψ_t and Δ_t are described from:

$$\rho_t = \frac{t_p}{t_s} = tan\Psi_t exp(i\Delta_t) \tag{4.2.5}$$

The ellipsometry parameters $\Psi_r(\Psi_t)$ and $\Delta_r(\Delta_t)$ are the amplitude ratio and phase difference for the reflection(transmission) coefficients respectively. The ellipsometer is a sensitive instrument employed for the optical characterization of thin films . The high sensitivity of the instrument has seen the areas of its application expanding also into the field of metamaterials[43, 44]. Nevertheless, the exploitation of ellipsometric techniques in metamaterial characterization is not very common. Including the angular-dependent response should give a much better optical characterization of a sample. The polarization state of light can be measured and from these the ellipsometer parameters Ψ and Δ are obtained. From the ellipsometric parameters, optical properties such as refractive index, permittivity, permeability and thickness of thin films, etc can be indirectly deduced from the fitting procedure. An estimator for a good fit between the model and the experimental data is the mean square error(MSE). The MSE is given by:

$$MSE = \frac{1}{2N-M}\sum_{i=1}^{N}\left[\left(\frac{\Psi_i^{mod}-\Psi_i^{exp}}{\sigma_{\Psi_i}^{exp}}\right)^2 + \left(\frac{\Delta_i^{mod}-\Delta_i^{exp}}{\sigma_{\Delta_i}^{exp}}\right)^2\right] \tag{4.2.6}$$

where N is the number of measured Ψ-Δ pairs, M is the number of fit parameters for the model, σ^{exp} is the standard deviation on the measured experimental data. The model and experimental data are represented by the superscripts *mod* and *exp* respectively. For the fitting model parameters, minimizing the MSE is a necessity for a reliable fit. The procedures involved in the measurements are outlined as follows

1. Measurement
    - A measurement of the sample is performed to determine the optical parameters. Since these optical parameters are not directly measured, the reflection coefficients, R, transmission T, and the ellipsometric Ψ and Δ as a function of beam wavelength or angle of incidence is measured.
2. Develop a Model
    - A model is fit to the measured data. The model generally contains unknown quantities such as thickness of the layer and optical constants.
3. Fitting of model to measurement
    - The unknown parameters are then varied and data are generated. These unknown parameters are optimized to give the generated data that matches(as close as possible) the measured data.
4. Best fit
    - A best fit set of unique parameters is then established

The basic parts or components of the ellipsometer are shown in Fig. 4.2. The beam from the monochromator (not shown) is channeled to the input unit through the optical fibre. The input unit contains the polarizer and autoretarder(wave plate) for controlling

polarization state of the input beam. The output arm contains a rotating analyzer and two detectors: for visible and NIR wave ranges. The computer controls data acquisition and elaboration.

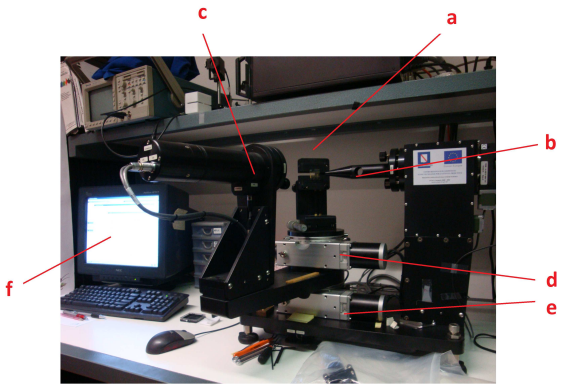

Figure 4.2: The VASE Ellipsometer. The parts of the instrument include: (a)sample stage, (b) input arm with focusing probe, (c) output arm, (d)and (e) are goniometer for angular control and (f) computer.

4.3 Substrate characterization

The dimer structure has been fabricated on two different substrates, silicon and a glass-ITO substrate respectively. To obtain good experimental results and fitting, we first characterize the bare substrates on which the pattern have been deposited, after which the actual fabricated dimer is characterized. In this section, we describe the method for the substrate characterization.

4.3.1 Glass-ITO substrate characterization

The experimental data for the glass-ITO substrate are obtained for angles of incidence varying from 20° to 70° with a step of 10°. The ellipsometer parameters Ψ and Δ are shown in Fig. 4.3 and Fig. 4.4.

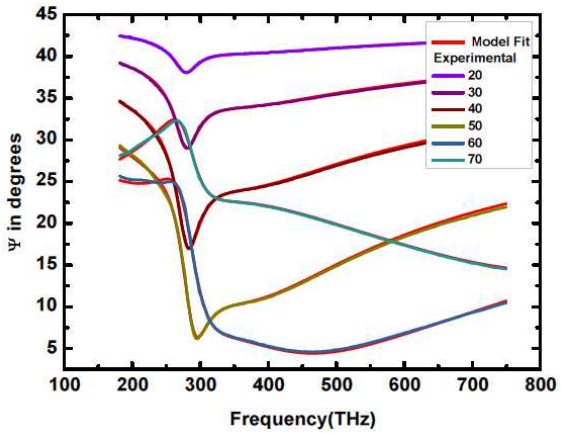

Figure 4.3: Experimental and fit data(red) of Ψ for the glass-ITO substrate for various angles of incidence.

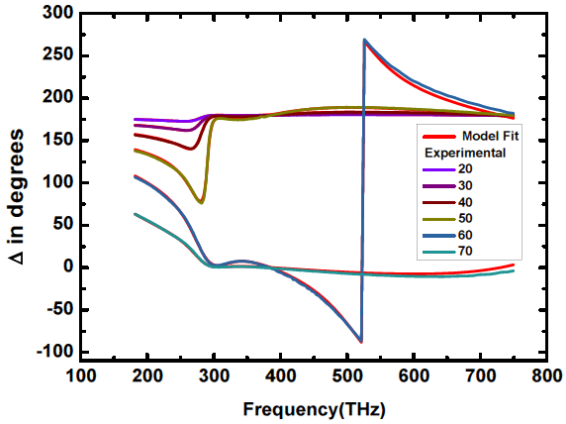

Figure 4.4: Experimental and fit data(red) of Δ for the glass-ITO substrate for various angles of incidence.

The optical model for this substrate is shown in Table 4.1. The substrate consists of the glass modelled as a Cauchy layer, a silicon dioxide layer Si02, and layer of ITO formed by two sublayers: "ITO A" and "ITO B". Note that ITO is inhomogeneous along z-direction because of complicated fabrication technique including evaporation and subsequent annealing processes.

The refractive index n and wavelength λ of light for a material are related by the Cauchy model, given by:

ITO B	19.0950 nm
ITO A	38.3823 nm
Si02	41.0109 nm
Cauchy	1mm

Table 4.1: Model for the glass-ITO substrate.

$$n(\lambda) = A + \frac{B}{\lambda^2} \tag{4.3.1}$$

where the coefficients A and B can be obtained from the fitting. The Cauchy parameters for the glass are $An = 1.4949$ and $Bn = 0.019918$. The parameters for the Si02 are taken from[45]. A Lorentz model is used to describe the "ITO A" and "ITO B" layers. The Lorentz model is given by:

$$\varepsilon(E) = \varepsilon_1(\infty) + \sum_{i=1}^{N} \frac{Am_i}{En_i^2 - E^2 - iBr_iE} \tag{4.3.2}$$

where $\varepsilon(E)$ is the photon energy E dependent dielectric function, N represents the total number of oscillators and $\varepsilon_1(\infty)$ is the real part of the dielectric function at very large photon energies. The other parameters describing the oscillator are the amplitude A_i, resonance position $En_i(eV)$ and broadening $Br_i(eV)$ for the i^{th} oscillator.

The "ITO A" layer is modelled with two Lorentz oscillators as shown in Table 4.2. The oscillator parameters are: $\varepsilon_1(\infty) = 3.2884$, $Am_1 = 5.3676$ $Br_1 = 0.19496$ and $En_1 = 0$ for the first oscillator. For the second oscillator, the parameters are: $Am_2 = 16.922$ $Br_2 = 1e-5$ and $En_2 = 4.8063$.

Am	Br(eV)	En(eV)
5.3676	0.19496	0
16.922	1e-5	4.8063

Table 4.2: Oscillator parameters for ITO layer A

Am	Br(eV)	En(eV)
1.569	2.5271	0
556.56	1e-5	9.8102

Table 4.3: Oscillator parameters for ITO layer B

The upper layer, "ITO B", was described with two Lorentz oscillators as shwon in Table 4.3, with $\varepsilon_1(\infty) = -2.7737$. The oscillator parameters $Am_1 = 1.569$ $Br_1 = 2.5271$ and $En_1 = 0$ for the first oscillator, while for the second oscillator we have $Am_2 = 556.56$ $Br_2 = 1e^{-5}$ and $En_2 = 9.8102$.

The experimental results and the fit were obtained with a fitting error of $MSE = 0.9$. In Fig. 4.3 and Fig. 4.4 the fitting curves obtained for the parameters Ψ and Δ are plotted, with both graphs showing a good agreement between the experimental data and the model. From this fit, the real and imaginary index, n and k is obtained for the substrate.

It is worth noting that the description of a metamaterial layer as a homogeneous layer with effective material parameters (EMP) is heavily debated in literature(see[44, 46]). Actually material parameters should be applicable to different wave processes in the sample independently of its shape, environment and kind of wave incidence. Very often this is not the case for metamaterial samples, for several reasons. First, long-

wavelength assumption implicit in applying EMP to metamaterials is generally violated, resulting in non-local electromagnetic response or spatial dispersion. The dependence of optical parameters on the wave-vector appears to increase for large angle of incidence on the metasurface. Second, optical properties of the metasurface strongly depend on the substrate characteristics. Hence, EMP obtained even for normal incidence can not be applied if one modifies complex permittivity of the substrate. Moreover, the replacement of the metasurface by a bulk layer with finite thickness is non-physical and usually the question arises as to which value of thickness must be ascribed to that layer. That is why we provide the thickness which satisfies the ellipsometric, reflectance and transmittance responses for the range of incidence angles simultaneously. Taking into account the above considerations, one can use the results obtained in this section for effective permittivity tensor either for simulation of metamaterial optical response for small angles of incidence or for illustration of plasmonic resonances occurred.

4.4 Determination of optical constant for Gold

In the previous section, we have obtained the optical constants for the glass-ITO substrate on which the metal nanostructures would be patterned. Here, we use the ellipsometer to determine the Drude parameters of the metal layer, in particular the collision frequency. That study was necessary since optical properties of thin metal films differ from those of a bulk metal because of the granular structure and enhanced effect of surfaces. A $30nm$ thin film of gold is evaporated onto a glass substrate. Experimental measurements were made for angles of incidences of $50, 60$ and 70° and the corresponding ellipsometric parameters, Ψ and Δ, were obtained. We put the upper limit of 1.5 eV to the spectral range of measurements to be consistent with Drude model for optical response of gold.

Also, transmittance at normal incidence was measured as shown in Fig. 4.5. Ellipsometric data Ψ and Δ are shown in Fig. 4.6 and Fig. 4.7 respectively.

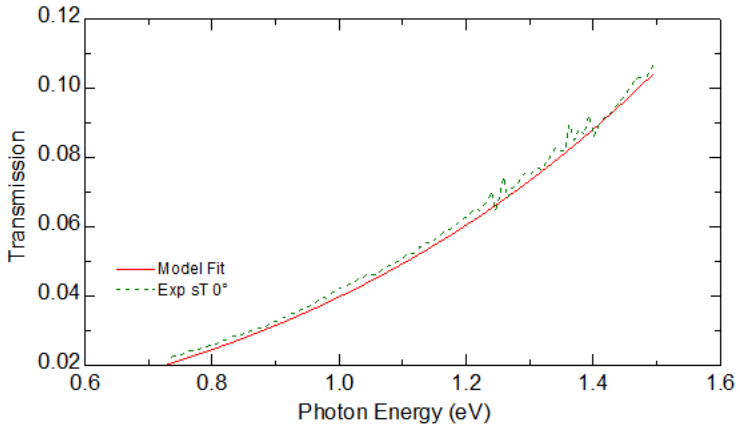

Figure 4.5: Experimental(green) and fit data(red) for transmission measurements for the gold film on the substrate.

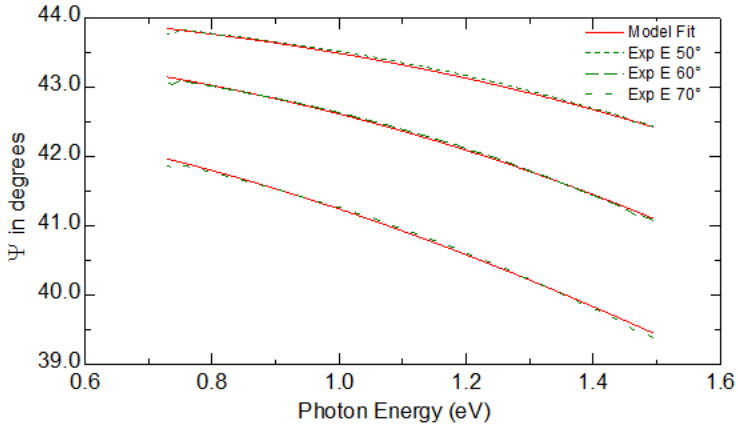

Figure 4.6: Experimental and fit data(red) of Ψ for gold on the glass-ITO substrate for various angles of incidence. From the fitting procedure, the optical parameters of the gold is extracted.

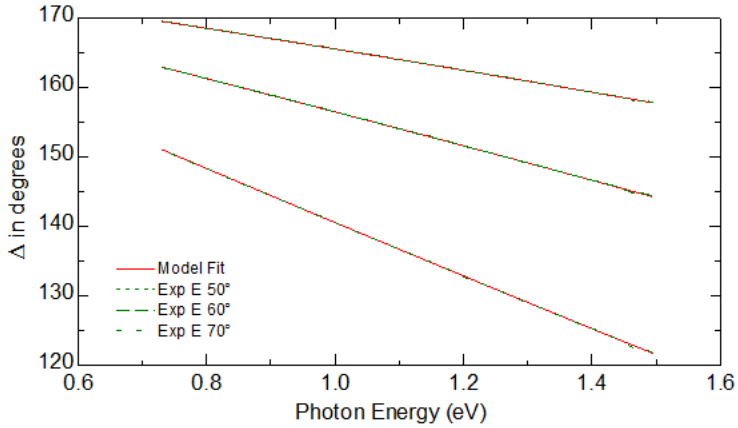

Figure 4.7: Experimental and fit data(red) of Δ for gold on the glass-ITO substrate for various angles of incidence.

The model is made up of a three layer material consisting of the glass substrate, the gold metal(Drude model layer) and some roughness layer(thus can be neglected as it appears from fit) as shown in Table 4.4.

The fitting parameters $\rho = 1.5011e^{-5}$, $\tau = 4.3077F$, thickness$= 27.1790nm$, with a fitting error of $MSE = 0.87$.

A version of the Drude model given by:

$$\varepsilon(E) = \frac{-\hbar^2}{\varepsilon_0 \rho (\tau \cdot E^2 + i\hbar E)} \tag{4.4.1}$$

2 Roughness	0.0000 nm
1 Drude model layer	27.1790nm
0 Glass	1mm

Table 4.4: Ellipsometer fitting parameters the metal thin film with gold(Drude model layer)deposited on a glass substrate.

where the resistivity $\rho(\Omega - cm)$is

$$\rho = \frac{m^*}{Nq^2\tau} = \frac{1}{q\mu N} \tag{4.4.2}$$

with scattering time τ(sec), carrier effective mass m^*, carrier concentration $N(cm^{-3})$, carrier mobility $\mu(cm^2V^{-1}s^{-1})$ and electron charge $q(1.6 \times 10^{-19})$. Comparing with equation. 4.4.1, the fitting parameters An and Br can be written as:

$$An = \frac{\hbar}{\varepsilon_0 * \rho} \tag{4.4.3}$$

and

$$Br = \frac{\hbar}{\tau} \tag{4.4.4}$$

where $\hbar$ is the reduced Planck's constant.

From these, the collision frequency for the gold is calculated as $\omega_c = 0.21 \times 10^{16} Hz$, thus the experimentally measured parameter being different from that previously used in simulations in Chapter 2. The plasma frequency was obtained from ellipsometric measurements to be in agreement with its value for bulk gold provided in literature. Thus, we simulated the spectral response considering different values for collision frequency which is proportional to losses in gold, depicted in Fig. 4.8(is repeated here

Fig. 2.24 for convenience).

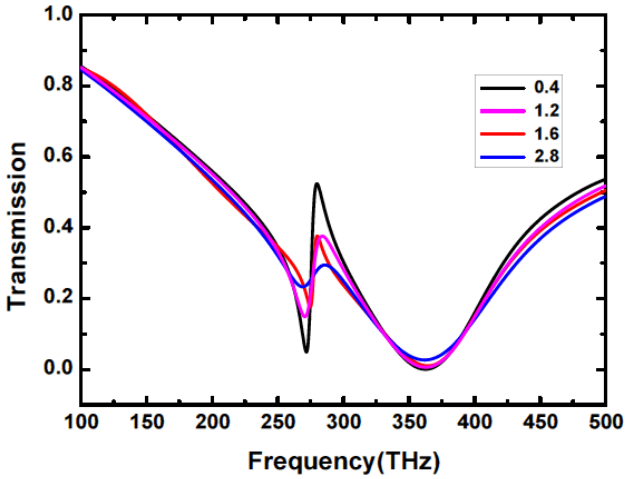

Figure 4.8: Spectral response for $\alpha = 30nm$ for losses Gold. The resonances are strongly affected by the losses with a decrease in amplitude from the theoretical case(black line).

With increasing losses, the amplitude of the bright and dark resonances both decrease. Also, there is a broadening of both resonances as well. However, the dark modes are more affected by this increase in metal losses, thereby showing much more broader resonance with increasing loss than the bright mode. However, the resonance position for the bright and dark modes are relatively unaffected by these metallic losses.

4.5 Dimer on glass substrate

In this section, we describe the optical characterization of the dimer using the Variable Angle Spectroscopic Ellipsometry(VASE). The sample measurements were done for various angles of incidence. The orientation of the dimer axis for the measurements were carried out for the cases with the dimer axis along and normal to the incidence plane. The reflection and transmission spectra and the ellipsometric spectra from the measurements were obtained, with results compared to the numerical spectral from simulation.

4.5.1 Intensity measurements for incidence plane along dimer axis

Experimental measurements were performed with the nanowires of the dimer oriented parallel to the plane of incidence shown in Fig. 4.9.

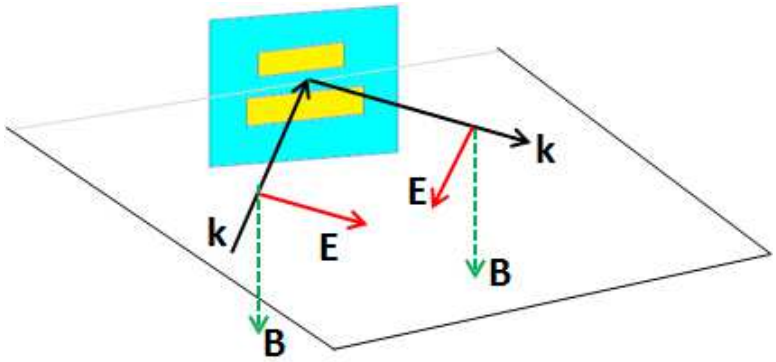

Figure 4.9: Dimer orientation with respect to incidence plane. Incidence plane is parallel to the nanowire lengths.

Reflection measurements were carried out for p-polarisation and s-polarisation for various angles of incidence. In reflection mode, the ellipsometer is limited to angle of incidence not smaller than 15°. In this set up, the incident electric field has the component oriented along the dimer axis for p-polarization measurements.

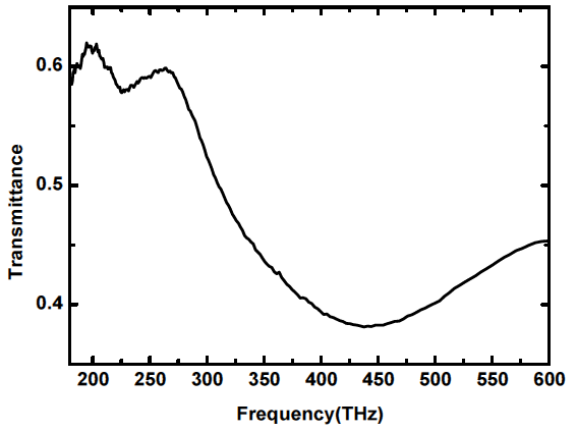

Figure 4.10: Measured Transmittance spectra for asymmetric dimer with $\alpha = 30nm$ at normal incidence. E field along nanowires.

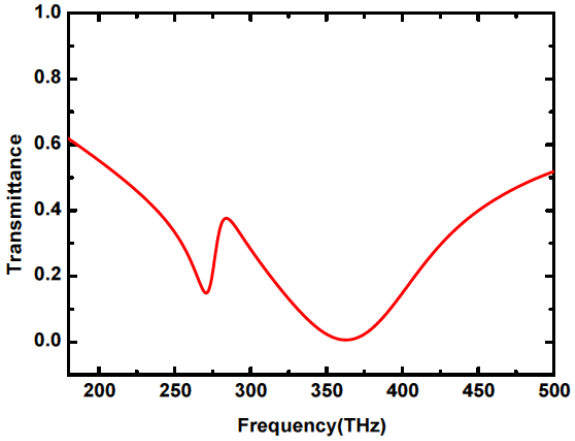

Figure 4.11: Simulated transmission for asymmetric dimer with $\alpha = 30nm$ at normal incidence. E field along nanowires.

The transmittance spectra for the asymmetric dimer with $\alpha = 30nm$ is represented in Fig. 4.10, for p-polarization. The sample was measured at normal incidence. Two resonance dips in transmission spectra can be observed. Comparing with the calculated spectra in Fig. 4.11, the observed modes correspond to both the dark and bright resonance. The expected dark modes in the experimental spectra is at a frequency of $226.3THz$ while the bright mode is at a frequency of $437.6THz$. The resonances show a generally good agreement with the calculated spectra. The discrepancy in the exact position of resonances can be attributed to the fabrication process, with slight variations in the statistical distribution of the dimensions of the nanowires, as shown in Table 4.5.

d	a1	a2	L1	L2	Px	Py
46.9						
51	82.3	84.4	191.7	226	311.4	305.2
42.7	77.1	87.5	189.6	226	317.7	309.4
38.5	84.4	78.1	200	228.1	317.7	309.4
41.7	82.3	80.2	200	228.1		
43.8	78.1	83.3	189.6	212.5		
44.8	85.4	80.2	190.6	220.8		
52.1	81.3	84.4	189.6	219.8		
39.6	83.3		192.7	220.8		
	81.3		183.3	214.6		
	88.5		183.3	211.5		
			186.5	211.5		
			181.3	216.7		

Table 4.5: Variation of the fabricated parameter dimensions for the nanostructure from simulation. All dimensions are in nm. d is the spacing between nanowires $L1$ and $L2$, $a1$ and $a2$ are the width of $L1$ and $L2$, Px and Py the period along x and y directions respectively.

The reflection spectra were also measured, as depicted in Fig. 4.12. As expected, the spectra shows reflectance peaks at the positions of the dark and bright modes. The sample was measured with angles of incidence from 15° to 30°, with an increment of 5°. Note that for off-normal incidence the resonances appear in the visible range($450 - 600THz$). These resonances are due to periodicity of the patterned structure(period about $300nm$) in analogy with Wood anomalies. They are sharp but their frequency depends strongly on the angle of incidence. A discussion on these resonances goes beyond the scope of this thesis.

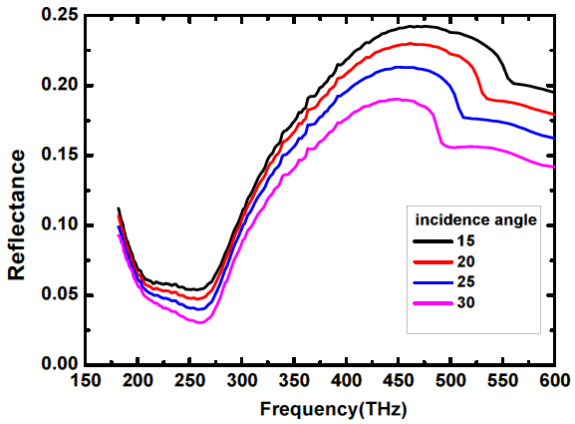

Figure 4.12: Reflectance spectra for asymmetric dimer with $\alpha = 30nm$, for angles of incidence from 15 to 30 degrees. E field along nanowires.

In Fig. 4.13 and Fig. 4.14, the spectra for the s-polarization transmission and reflection

spectra respectively are plotted. The s-polarized transmission and reflection spectra do not show any resonances for the dark and bright modes, as expected.

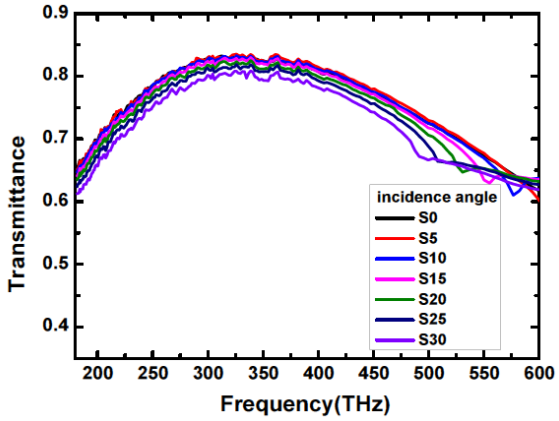

Figure 4.13: Transmittance spectrum for s-polarization in asymmetric dimer with $\alpha = 30nm$ and with incidence plane parallel to the dimer axis.

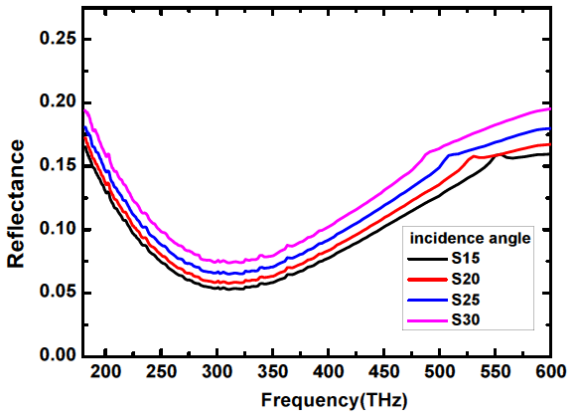

Figure 4.14: Reflectance spectrum for s-polarization in asymmetric dimer with $\alpha = 30nm$ and with incidence plane parallel to the dimer axis

The absorption for the p and s-polarization as calculated from the data for reflectance and transmittance, are shown in Fig. 4.15 and Fig. 4.16 respectively. For p-polarization, two absorption peaks are noticeable at the resonance position for the dark and bright modes, whereas for the s-polarization, no absorption peaks can be observed.

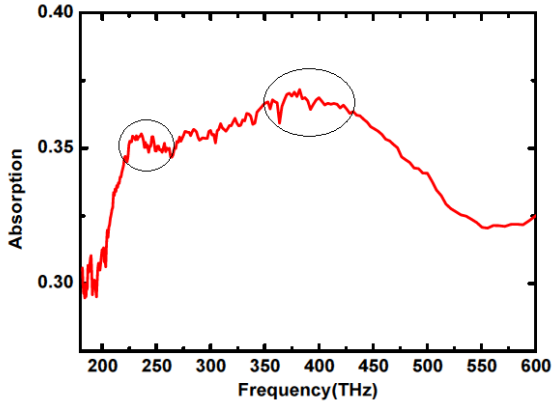

Figure 4.15: Absorption spectrum for p-polarization in asymmetric dimer with $\alpha = 30nm$ for incidence plane parallel to the dimer axis. Absorption peaks appear at the dark and bright mode resonances of $226.3THz$ and $437.6THz$ respectively.

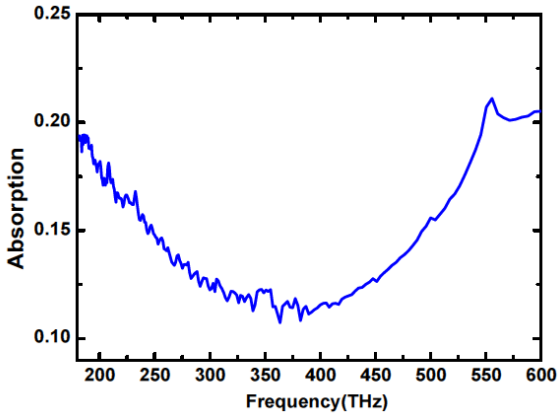

Figure 4.16: Absorption spectrum for s-polarization in asymmetric dimer with $\alpha = 30nm$ for incidence plane parallel to the dimer axis. There are no absorption peaks for this polarization.

4.5.2 Intensity measurements for incidence plane perpendicular to dimer axis

The measured sample in the previous section was for the case where the dimer axis is along the incidence plane. In the following measurements, the sample is oriented such that the dimer axis is normal to the incidence plane(see Fig. 4.17). The ellipsometer measures both the s- and p-polarization components of the reflection and transmission. For the p-polarised measurements, the electric field component of the wave is normal to the dimer axis whereas for the s-polarization measurements, the electric field component is along the dimer axis.

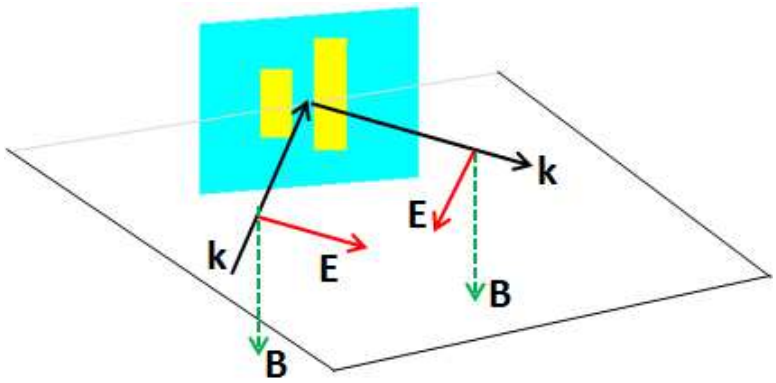

Figure 4.17: Dimer orientation with respect to incidence plane. Incidence plane is perpendicular to the nanowire lengths.

The experimental data for oblique reflection measurements for both p-and s-polarisations for various angles of incidences from 15° to 30° is shown in Fig. 4.18 and Fig. 4.19 respectively.

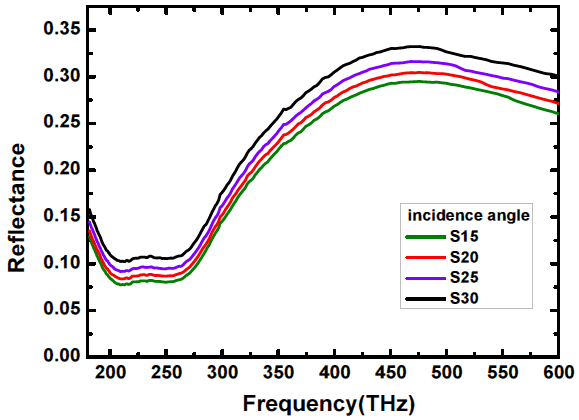

Figure 4.18: Reflectance spectrum for s-polarization in asymmetric dimer with $\alpha = 30nm$ and with incidence plane perpendicular to the dimer axis.

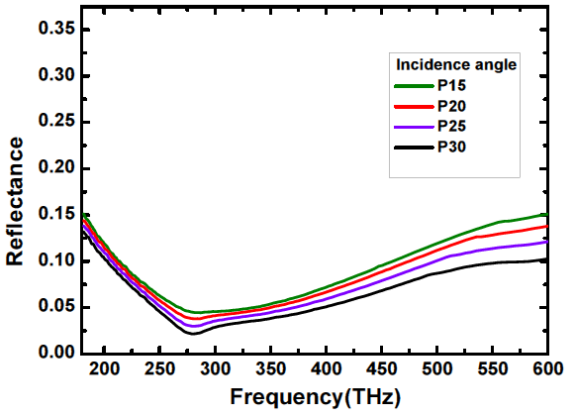

Figure 4.19: Reflectance spectrum for p-polarization in asymmetric dimer with $\alpha = 30nm$ and with incidence plane perpendicular to the dimer axis.

For the s-polarisation measurements at incidence angle of 15 degrees, two resonances appear at 229.5THz and 464.8THz. These resonances are the dark and bright modes respectively. These resonances are similar to those described in Fig. 4.12 where the incidence plane is along the dimer axis. The small difference in the resonance position is due to the accuracy in aligning the sample to the incidence plane after orientation. Nonetheless, both results are still consistent and in agreement with numerical simulation. For the p-polarized measurements in Fig. 4.19, no resonances are obtained, which is consistent with the measured reflectance spectra for the s-polarized reflection for the case where the incidence plane is along the dimer axis in Fig. 4.14.

Likewise, the measured experimental transmission data for this orientation for normal incidence is shown in Fig. 4.20. The dark and bright resonances are at 229.5THz and 440.8THz, respectively, consistent with calculated spectrum. Moreover, for off normal angles of incidence, from 5° to 30°, the resonance positions are at about the same position as depicted in the measured spectra in Fig. 4.21.

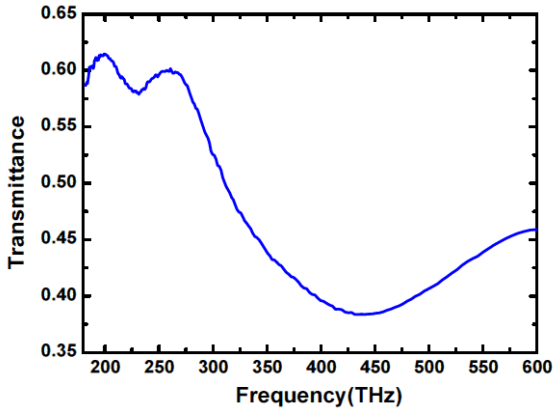

Figure 4.20: Transmittance spectra for asymmetric dimer with $\alpha = 30nm$, for normal incidence.

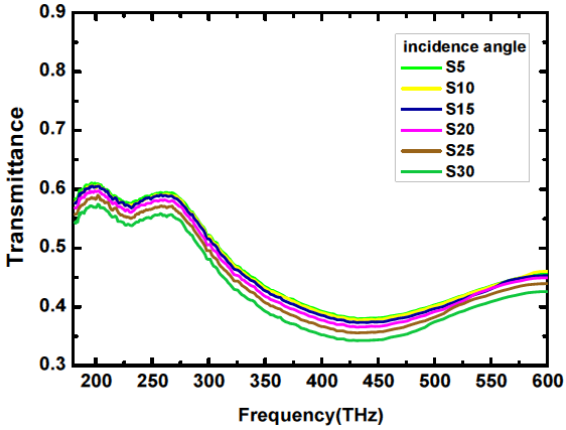

Figure 4.21: Transmittance spectra for asymmetric dimer with $\alpha = 30nm$, for angles of incidence from 5° to 30°.

4.5.3 Ellipsometric measurements and determination of effective parameters for the metamaterial layer

Having described the resonances in the dimer from the measured intensity in transmission and reflection modes with the incidence plane normal and perpendicular to the dimer axis, we proceed to model the optical response of the structure using ellipsometric techniques described in section 4.2. The glass-ITO substrate model and fit has been described in previous section and the obtained optical constant and thicknesses of the substrate layers are used here. The model and fitting procedure is done considering the presence of the gold dimer nanostructure on the glass-ITO substrate. The optical response of the nanostructure is described as a continuous layer "Metalayer", with a thickness t. Considering that the response depends on polarization of incident electromagnetic field(see sections 4.5.1and 4.5.1), a biaxial dielectric tensor $(\varepsilon_x, \varepsilon_y, \varepsilon_z)$ is used for describing effective material parameters of this layer. Table 4.6 shows the layer model for the asymmetric dimer with $\alpha = 30nm$. It is worth noting that it is not possible extract simultaneously both imaginary part of permittivity and the thickness for the absorbing layer. That is why we fit ellipsometric data together with transmittance and reflectance measurements to obtain the effective thickness of the Metalayer.

Metalayer	16.3406 nm
ITO B	19.0950 nm
ITO A	38.3823 nm
Si02	41.0109 nm
glass	1 mm

Table 4.6: Optical model for the dimer.

The experimental data and simulated curves are shown in Fig. 4.22 and Fig. 4.23 for ellipsometric parameters Ψ and Δ respectively, for small angles, and Fig. 4.24 and Fig. 4.25 for larger angles respectively, and in Fig. 4.26 and Fig. 4.27 for the transmittance and reflectance respectively for a mean square error of fit $MSE = 0.6736$. A good fit is observed between experimental and model curves(red) for small angles of incidence. Insufficient fit for larger angles and high frequencies can be caused by increasing effect of spatial dispersion.

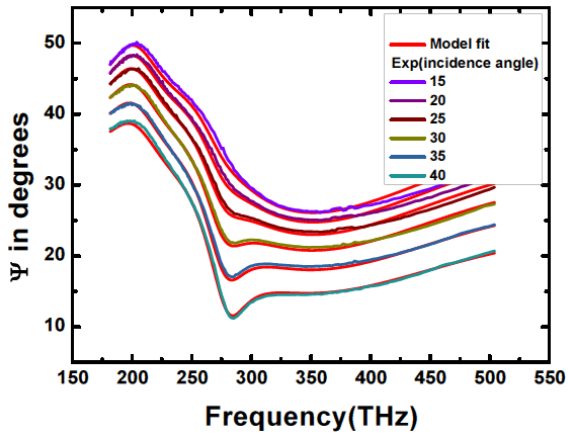

Figure 4.22: Experimental and fit data(red) for ellipsometer parameter Ψ for dimer with $\alpha = 30nm$.

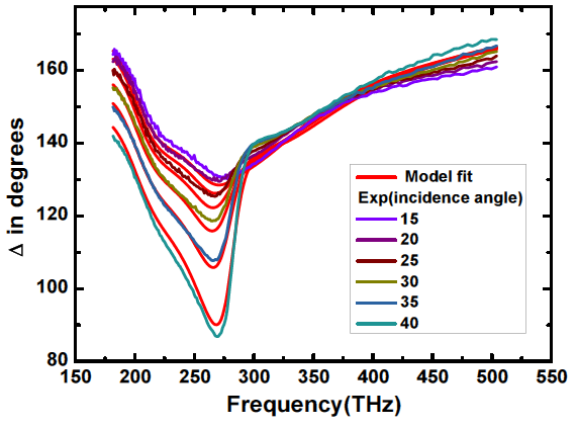

Figure 4.23: Experimental and fit data(red) for ellipsometer parameter Δ for dimer with $\alpha = 30nm$.

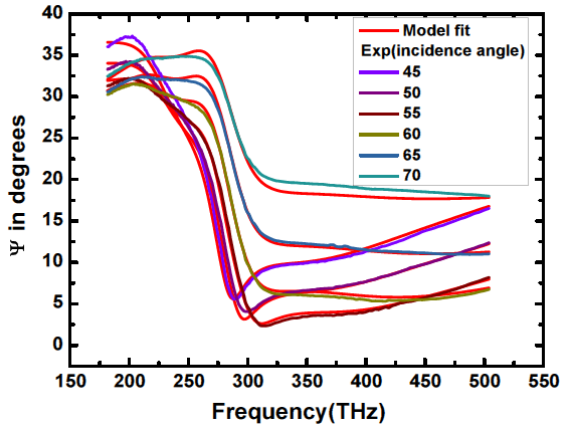

Figure 4.24: Experimental and fit data(red) for ellipsometer parameter Ψ for dimer with $\alpha = 30nm$ for larger angles.

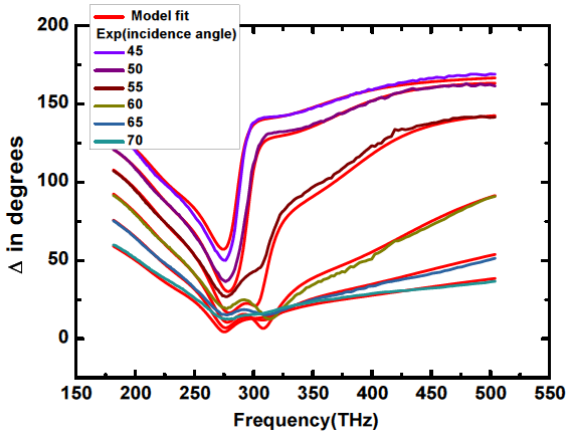

Figure 4.25: Experimental and fit data(red) for ellipsometer parameter Δ for dimer with $\alpha = 30nm$ for larger angles.

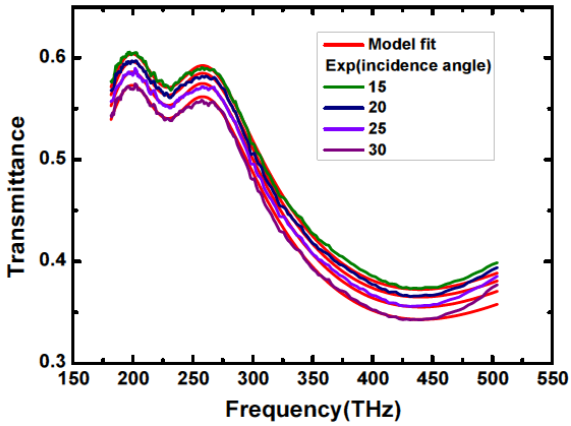

Figure 4.26: Experimental and fit data(red) for transmittance for dimer with $\alpha = 30nm$.

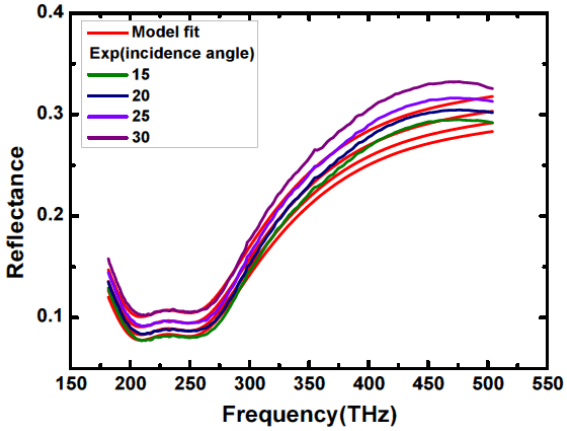

Figure 4.27: Experimental and fit data(red) for reflectance for dimer with $\alpha = 30nm$.

From the model fit, the dielectric constants for the nanostructure are extracted. The real and imaginary part of the permittivity tensor components are given in Fig. 4.28 and Fig. 4.29 respectively. Being extracted from the Lorentz oscillator model, real and imaginary parts of permittivity are Kramers-Kronig consistent so we explain below the physical meaning of the imaginary part only, which is closely related to plasmonic resonances in the patterned gold layer. The y-component of the permittivity tensor describes electromagnetic response for the field oriented along nanowire axis. It reveals two main resonance peaks at 230 and $400THz$ which correspond to strongly absorbing dark and bright modes respectively. Whereas the x-component characterizes small absorption due to the plasmonic oscillations across nanowires which have resonance

frequency about three time higher than longitudinal oscillations, i.e. over $700THz$. The x-component curve corresponds to the tail of these resonances. The most unexpected behaviour appears for z-component. This component has moderate and wide absorption maximum centered at $350THz$. Note that it cannot be due to the plasmonic oscillations in z direction because small thickness of the gold layer together with anti-bonding plasmon hybridization would provide much higher resonance frequency. The nature of z-component behaviour needs more investigation.

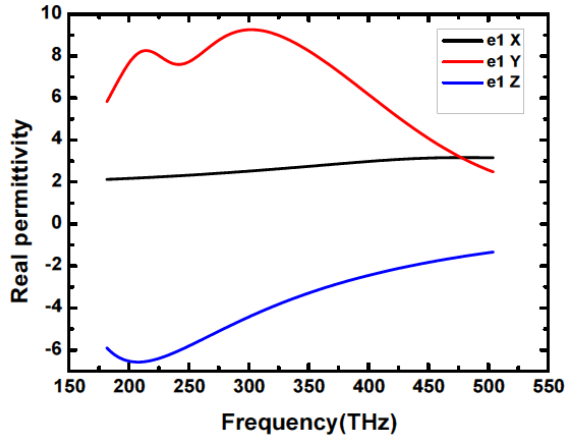

Figure 4.28: Real components of Permittivity.

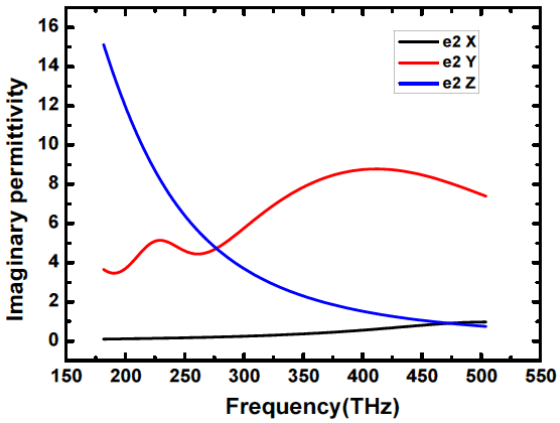

Figure 4.29: Imaginary components of permittivity.

It is worth noting that describing of metamaterial layer as a homogeneous layer with the effective material parameters (EMP) is heavily debated in literature[44, 46]. Actually material parameters should be applicable to different wave processes in the sample

independently of its shape, environment and kind of wave incidence. Very often it is not the case for metamaterial samples for several reasons. First, long-wavelength assumption implicit in applying EMP to metamaterials is generally violated which results in non-local electromagnetic response or spatial dispersion. The dependence of optical parameters on the wave-vector appears increasing for large angle of incidence on the metasurface. Second, optical properties of the metasurface strongly depend of those of the substrate. Hence EMP obtained even for normal incidence can not be applied if one modifies complex permittivity of the substrate. Moreover, the replacement of the metasurface by a bulk layer with finite thickness is non-physical and usually the question arises which value of thickness must be ascribed to that layer. That is why we provide the thickness which satisfies to ellipsometric, reflectance and transmittance responses for the range of incidence angles simultaneously. Taking into account the above one can use obtained in this section effective permittivity tensor either for simulation of metamaterial optical response for small angles of incidence or for illustration of plasmonic resonances occurred.

4.6 Dimer on Silicon substrate

4.6.1 Silicon Substrate characterization

In this section, we characterize the fabricated nanostructures on a silicon substrate. Since silicon substrate is not transparent in the wave range under study, we performed the reflection measurements only.

For small angles of incidence of 15°, the measured reflectance spectra for p- and s-polarizations are shown in Fig. 4.30. In the case of p-polarization with electric field parallel to nanowires of dimer(red curve), one peak of reflectance is observed at about

220THz, which is close to the simulated resonance frequency of the bright mode shown in Fig. 4.31.

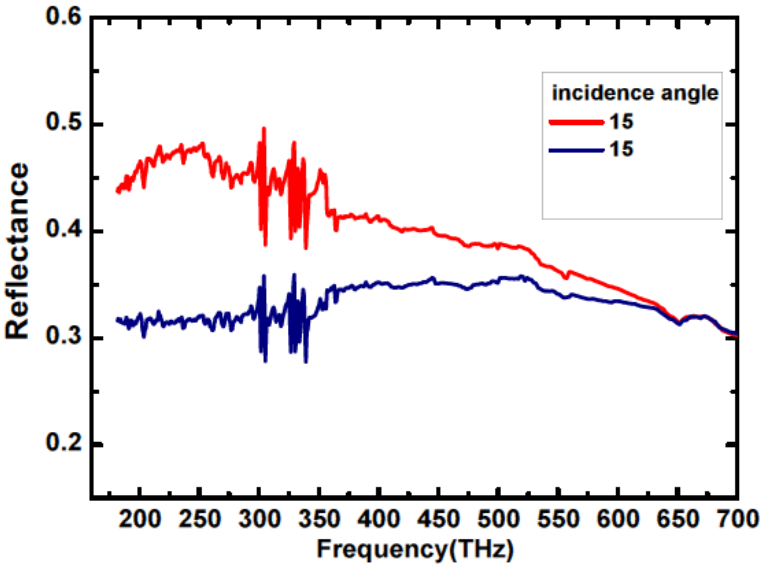

Figure 4.30: Experimental Reflectance amplitude for asymmetric dimer with length parameter $\alpha = 30nm$, on a silicon substrate for p-polarization(red) and s-polarization(blue) for an incidence angle of 15°.

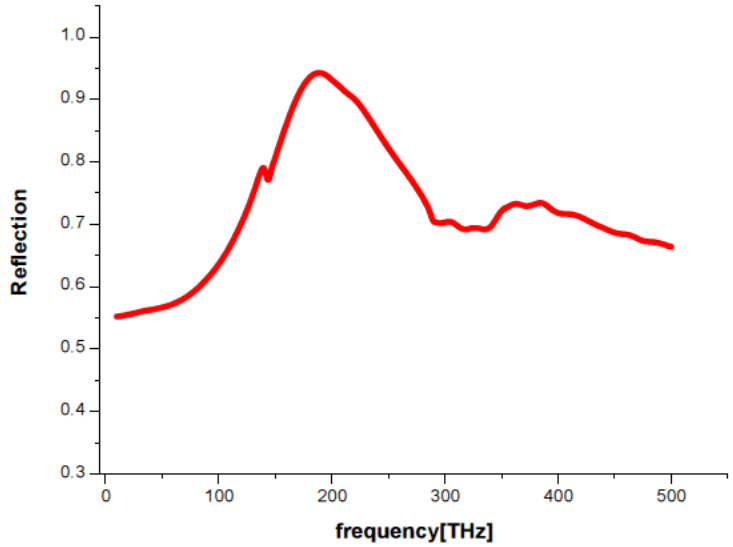

Figure 4.31: Simulated Reflection amplitude for asymmetric dimer with length parameter $\alpha = 30nm$, on a silicon substrate.

From the numerical calculated reflection spectrum in Fig. 4.31, the dark and bright resonances are at 138.4THz and 188.5THz respectively, for the asymmetric dimer with a length parameter $\alpha = 30nm$ on a silicon substrate. The experimental resonance

at 220THz in the asymmetric dimer appears to not depend on the incidence angle. Though, the nature of this resonance is not clearly understood at this point since lower frequency measurements are required for a complete analysis. Therefore, we can not experimentally study the bright mode and especially the dark one because of the ellipsometer frequency range is limited to 180THz.

CHAPTER 5

Conclusion and Future work

5.1 Optical sensing with the dimer

The resonant frequency of the dimer is highly dependent on the size dimensions of the nanowire. The dependence of the spectral position of resonance on the permittivity of the surrounding medium is essential for any refractive index sensing device, with the sharp nature of the Fano-like resonances making them interesting for such applications. Optical sensing of materials is an area that is of broad interest, given the many possible applications of sensors in security, detection of biochemical substances, etc. Various configurations of sensors based on metamaterials have been presented in literature with different nanocomponents ranging from gold nanoparticles to nanodisks, pillars, etc.[47–49]. Typically, high sensitivity sensors are more desirable as they are more responsive to minute changes in the dielectric environment[50–52]. The behaviour of the dimer resonances under a varying dielectric environment can provide useful information with a view of its possible application as a sensing device. To investigate the applicability of the structure as a sensor, the dimer is coated with a dielectric liquid(pink) as shown in the cross section in Fig. 5.1. Varying the dielectric environment around the dimer, the response of the dark and bright modes to these changes for various length asymmetries is investigated.

Figure 5.1: Cross section of the dimer in a dielectric environment(pink) of varying index.

With $\alpha = 20nm$, the response of the dimer to a changing index around the dimer from $n = 1.1$ to 1.3 is calculated, as shown in the spectrum of Fig. 5.2. With an index of $n = 1.1$, the resonance spectrum redshifts for both bright and dark modes. The bright mode shifts from 355 to $348THz$ while the dark mode shifts from 266 to $260THz$. Further changing the index of the dielectric environment from $n = 1$ to $n = 1.2$, the resonances down shift in frequency for bright mode to $343THz$ and $253THz$ for the dark mode respectively. A further increase of the index to $n = 1.3$ similarly downshifts the bright and dark modes to $338THz$ and $247THz$ respectively(see Fig. 5.2).

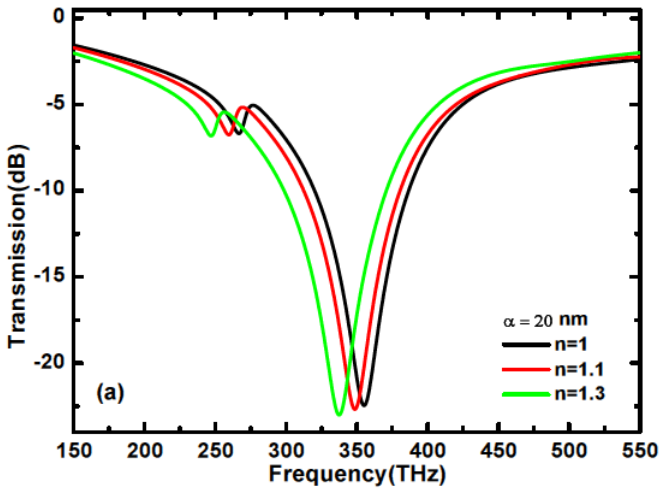

Figure 5.2: Spectral shifts in resonance for $\alpha = 20nm$ for changes in the index of the dielectric material surrounding the dimer metamaterial.

From this response of the modes to changes in the dielectric environment, we can evaluate the sensitivities of the dark and bright modes respectively. The sensitivity S, is usually defined as the ratio of the change in wavelength$\Delta\lambda$ to the change in refractive

index Δn.

$$S = \frac{\Delta\lambda}{\Delta n} \tag{5.1.1}$$

The unit of the sensitivity is nm/RIU, where RIU is the refractive index unit. For $\alpha = 20nm$, Fig. 5.3 shows the spectral shifts in wavelength $\Delta\lambda(nm)$ for the changes in the refractive index n of the dielectric medium surrounding the dimer.

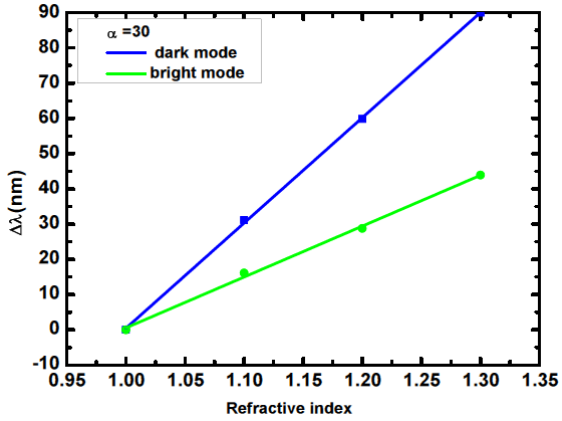

Figure 5.3: Sensitivity response for $\alpha = 20nm$ with varying index.

From the calculated frequency responses to the dielectric changes in Fig. 5.3, the sensitivity for the respective bright and trapped mode resonances is evaluated. For the dark mode, $S = 300.1nm/RIU$ while for the bright mode $S = 146.3nm/RIU$.

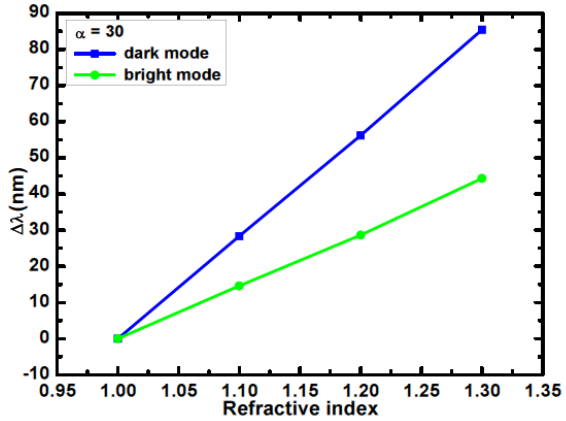

Figure 5.4: Sensitivity response for $\alpha = 30nm$ with varying index.

In a similar analysis, the respective spectra for $\alpha = 30nm$ and $\alpha = 40nm$ for changes in index n from 1.1 to 1.3 is calculated. Fig. 5.4 shows the spectral changes to this variation for an asymmetry parameter of $\alpha = 30nm$ and the calculated sensitivities for the dark and bright modes are $S = 284.7nm/RIU$ and $S = 147.5nm/RIU$ respectively.

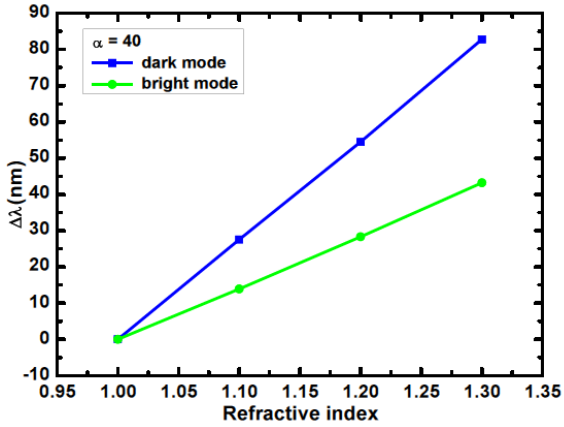

Figure 5.5: Sensitivity response for $\alpha = 40nm$ with varying index.

For $\alpha = 40nm$, Fig. 5.5 shows the spectral changes to index variation at resonance, with the dark and bright modes having sensitivities $S = 276.1nm/RIU$ and $S = 144.0nm/RIU$ respectively.

Therefore from the numerical results, the dark modes show a generally higher sensitivity compared to the bright modes under the same index variation. This characteristic behaviour to changes in dielectric environment is advantageous as it offers the possibility of exploiting it for the development of a functional sensing device. Thus, for the purpose of sensing we can concentrate on the dark modes. Keeping in mind sensing is a possible application, we have to concentrate on the effects of the dark mode properties.

Length asymmetry(nm)	Sensitivity (nm/RIU) Dark(bright)	FOM (RIU^{-1}) Dark(bright)
20	300.1 (146.3)	7.0 (3.0)
30	284.7 (147.5)	5.2 (3.0)
40	276.1 (144.0)	4.1 (3.0)

Table 5.1: Sensitivity and Figure of merit(FOM) to changes in dielectric environment for dimers with length asymmetry $\alpha = 20, 30, 40nm$

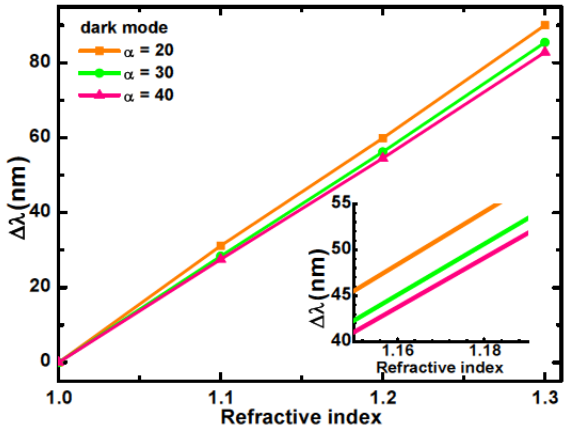

Figure 5.6: Dark mode sensitivity response for values of $\alpha = 20, 30 and 40nm$.

The response of the dark modes to these index changes appears to depend on the asymmetry parameter, α. In Fig. 5.6, the sensitivities only at various values of α for the dark modes is plotted. Low α values(smaller length asymmetry), give a higher response to changes in the index of the dielectric environment. This behaviour can be explained by the reduction of the electromagnetic field concentration at the metasurface with increasing length asymmetry, which is confirmed by the lowered Q value(Fig. 2.25).

To compare the sensing performance of spectroscopic sensors operating at different

wavelengths, the figure of merit (FOM) appears to be a more effective parameter than sensitivity. FOM is defined as the sensitivity divided by the resonance width and it is therefore inversely proportional to the smallest detectable refractive index change at the sensor output(resolution)[53, 54], given as:

$$FOM = \frac{sensitivity}{\Delta\lambda} \tag{5.1.2}$$

The FOM values for the dark mode at different values of length asymmetry $20, 30$ and 40 nm are $7.0, 5.2$, and $4.1 RIU^{-1}$ respectively. The FOM is much lower for the bright mode, staying approximately constant at $0.3 RIU^{-1}$(see Table 5.1). Hence, the dark mode in the dimer appears more suitable for the development of a simple spectroscopic sensor, given the high values of both sensitivity and figure of merit. Conventional surface plasmon resonance sensors have FOM much larger, in the range of 80, however at the expense of a higher complexity since they rely on the use of prisms or gratings to couple the impinging light to the surface plasmon. It is worth to emphasize that provided FOM values in the asymmetric dimer configuration are larger than those for an array of spherical gold nanoparticles with comparable dimensions(particle diameter and lattice period)[55].

5.1.1 Dimer resonance in anisotropic environment

So far, in the previous section, we have investigated the resonance response behaviour of the asymmetric dimer metamaterial in a changing dielectric environment, with a potential towards its use as a sensor. However, for many applications tunable optical devices are desirable, whereby the resonance can be controlled. With active devices, tunability can be achieved. For example, using a semiconductor, it has been

experimentally demonstrated that a tunable metamaterial can be realized[56]. Here, the semiconductor was incorporated into the metamaterial and by photoexcitation, tuning of the resonance was achieved. Aside from using semiconductors for tunable metamaterials[57, 58], other materials have also been employed. Among these materials are liquid crystals(LC)[59, 60]. Liquid crystals posses properties of liquid and crystalline phase of matter and are also temperature dependent. The molecules of a liquid crystal have the ability to align in a preferential direction called the director[61]. The birefringent nature of LC makes them a suitable candidate to be employed for tunable materials and devices. Under an external field, the molecular orientation of the LC can be controlled and thereby offering the possibility of tunability due to the resulting change in the index[62–68]. In the presence of external fields, the molecules of the liquid crystals show a preferential orientation along the director, consequently the refractive index of the medium varies depending on the director orientation. In simulations, the dimer metamaterial is infiltrated with an $E7$ liquid crystal, which is commercially available, with the following characteristics for the ordinary n_o and extraordinary n_e index at room temperature for the Infrared region(IR)[69]: $[n_e = 1.69]$ and $[n_o = 1.5]$. An external electromagnetic field is used to reorient the director along either the x, y or z axis. We show two possible cases: (i) LC orientation is parallel to the dimer axis; (ii) LC orientation is normal to the dimer plane. In the calculations, some assumptions have been made. We assume that the field is strong enough to align all the molecules of the liquid crystal. Also, the surface anchoring effect has been neglected. The surface anchoring effect is the tendency of the LC molecules to have a particular orientation due to contact with the surface of the nanoparticles[70–72]. In both configurations, the polarization of the incident field is along the long axis of the dimer as depicted in Fig. 5.7 and Fig. 5.8. The incident field responds to different index

depending on the director orientation.

(i) Director orientation parallel to Dimer axis

For a director orientation along the x axis, the incident field feels the extraordinary index n_e of the LC, whereas along the y and z directions it feels the ordinary index n_o. Thus, we can write the index for this LC director orientation in the dimer as $[n_x, n_y, n_z] = [n_e, n_o, n_o]$ or since we are using in simulations $E7$, $[n_x, n_y, n_z] = [1.69, 1.5, 1.5]$. The response of the dimer to this director orientation is shown in Fig. 5.9(blue curve). Compared to the resonance response of the dimer in vacuum,(red curve of Fig. 5.9), we can clearly distinguish the shifts in the resonances due to the influence of the LC director orientation. The resonances for both bright and dark modes are red shifted with respect to the case without LC. In this orientation, the incident field experiences a higher effective index η_{eff} and thus downward shifts in the resonance. The dark mode resonance shifts from $271THz$ without LC to $232THz$ with the LC director orientation along x and likewise, the bright mode resonance shifts from $363THz$ to $324THz$ respectively.

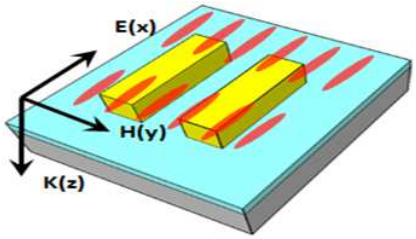

Figure 5.7: Asymmetric dimer with liquid crystal oriented along dimer axis.

(ii) Director orientation normal to Dimer axis

The LC director can be oriented to be normal to the plane containing the dimer, as shown in Fig. 5.8. With the director orientation along the z axis, the incident field

(polarization along the X axis) experiences the ordinary index n_o. Along the y and z axis is the ordinary n_o and extraordinary n_e indices respectively. Thus, we can write the index as $[n_x, n_y, n_z] = [n_o, n_o, n_e] = [1.5, 1.5, 1.69]$. The resonance response for this director orientation is shown in Fig. 5.9(green curve).

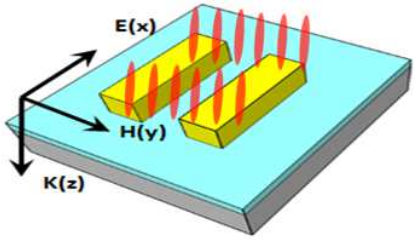

Figure 5.8: Asymmetric dimer with liquid crystal oriented normal to dimer axis.

The transmission spectra show a redshift for both dark and bright modes(green curve) in the presence of LC, compared to the case without LC(red curve). The dark mode resonance shifts to $237THz$ from $271THz$ while the bright mode resonance shifts from $363THz$ to $332THz$. Hence, as with the case of the director along the dimer axis(Fig. 5.9 blue curve), resonance shifts are observed for the director normal to the dimer plane(Fig. 5.9 green curve). However, the shifts are not of the same rate for the LC orientations. For the LC director along the dimer axis(Fig. 5.7), a higher shift in the resonance is observed compared to when the LC director in normal to the director axis(Fig. 5.8). This is shown in Fig. 5.9, where the spectrum shows a higher shift in resonance for the director orientated along the dimer axis(blue curve) than with the director orientation normal to dimer axis(green curve). Using LC we can dynamically control the response of the metamaterial dimer. This behavior of the resonances to the dimer orientation is due to the birefringent $\Delta n = n_e - n_o$ nature of the liquid crystal. Thus a larger degree of tuning can be realized with a liquid crystal of higher birefringence[73, 74].

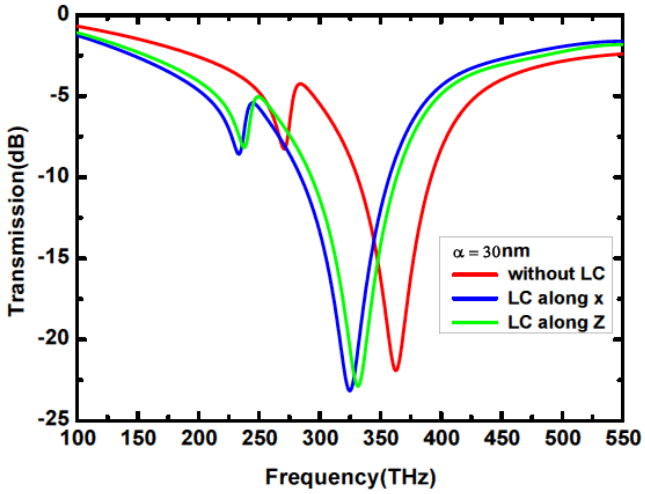

Figure 5.9: Transmission spectra for the Asymmetric dimer with $\alpha = 30nm$.

In conclusion, we have investigated the effect of symmetry breaking in the plasmonic dimer nanostructures. Calculated distributions of electric field and current at the surface of metallic nanorods reveal excitation of radiant and subradiant modes in the dimer. Both constructive and destructive interference between these modes results in Fano-type resonance in transmission spectra of the planar metamaterial on the base dark and bright mode coupling. The dominant factor in the excitation of the dark modes, the introduction of asymmetry in the length of the nanorod dimer, is independent of the way it is generated, rendering this metamaterial very robust to fabrication defects or other structural imperfections. The sensitivity of the dark resonances to the external dielectric environment of metasurface has been studied as well. The obtained sensitivity and figure of merit values are promising for the possible application of this simple planar nanostructure as a chemical or biological sensor. Optical characterization of the fabricated nanostructure was carried out using spectroscopis ellipsometry. The measured experimental results show good agreement with the simulation. Optical models for the dimer was constructed and dielectric parameters retrieved from the ellipsometer parameters Ψ and Δ.

5.2 Future work

Given the sensitive nature of the dark modes, the resulting sensor has been shown to be very sensitive to very minute amount of refractive index changes of the ambient environment around the nanodimer. Functionalizing the dimer metamaterial is essential as this opens up the possibilities to apply the metamaterial for index specific sensing. Overcoming this drawback is a big step towards achieving this goal and thus a possible research focus. A foreseen challenge is the possibility of a reusable sensor.

Bibliography

[1] E. Ozbay. "The magical world of photonic metamaterials". *Optics Photonics News*, 19(11):22 – 27, 2008.

[2] V. G. Veselago. "Electrodynamics of substances with simultaneously negative values of sigma and mu". *Sov Phys Usp*, 10:509–514, 1968.

[3] D. R. Smith, W. J. Padilla, D. C. Vier, S. C. Nemat-Nasser, and S. Schultz. "Composite medium with simultaneously negative permeability and permittivity". *Phys. Rev. Lett.*, 84:4184–4187, 2000.

[4] M. Gokkavas, K. Guven, I. Bulu, K. Aydin, R. S. Penciu, M. Kafesaki, C. M. Soukoulis, and E. Ozbay. "Experimental demonstration of a left-handed metamaterial operating at 100 ghz". *Phys. Rev. B*, 73(19):193103, 2006.

[5] D. Schurig, J. J. Mock, and D. R. Smith. "Electric-field-coupled resonators for negative metamaterials". *Appl. Phys. Lett.*, 88(4):041109, 2006.

[6] J. B. Pendry. "Negative refraction makes a perfect lens". *Phys. Rev. Lett.*, 85:3966 – 3969, 2000.

[7] R. A. Shelby, D. R. Smith, and S. Schultz. "Experimental verification of a negtive index of refrction". *Science*, 292:77–79, 2001.

[8] S. Linden, C. Enkrich, M. Wegener, J. Zhou, T. Koschny, and C.M. Soukoulis. "Magnetic response of metamaterials at 100 terahertz". *Science*, 306:1351, 2004.

[9] J. Zhou, Th. Koschny, M. Kafesaki, E. N. Economou, J. B. Pendry, and C. M. Soukoulis. "Saturation of the magnetic response of split-ring resonators at optical frequencies". *Phys. Rev. Lett.*, 95(22):223902 – 223904, 2005.

[10] M. W. Klein, C. Enkrich, M. Wegener, C. M. Soukoulis, and S. Linden. "Single-slit split-ring resonators at optical frequencies: limits of size scaling". *Opt. Lett.*, 31(9): 1259, 2006.

[11] U. Fano. "Effects of configuration interaction on intensities and phase shifts". *Phys. Rev.*, 124:1866 – 1878, 1961.

[12] S. E. Harris. "Electromagnetically induced transparency". *Phys. Today*, 50:36–42, 1997.

[13] V. M. Shalaev. "Optical negative-index metamaterials". *Nat. Photonics*, 1:41–48, 2007.

[14] Z. Haoa, M. C. Martinb, B. Harteneck, S. Cabrini, and E. H. Anderson. "Negative index of refraction observed in a single layer of closed ring magnetic dipole resonators". *App. Phys. Lett.*, 91:253119, 2007.

[15] A. Alù, A. Salandrino, and N. Engheta. "Negative effective permeability and left-handed materials at optical frequencies". *Optics Express*, 14:1557, 2006.

[16] E. Plum, X.-X. Liu, V. A. Fedotov, Y. Chen, D. P. Tsai, and N. I. Zheludev. "Optical activity without chirality". *Phys. Rev. Lett.*, 102:113902, 2009.

[17] A. Christ, O. J. F. Martin, Y. Ekinci, N. A. Gippius, and S. G. Tikhodeev. "Symmetry

breaking in a plasmonic metamaterial at optical wavelength". *Nano Lett.*, 8(8): 2171–2175, 2008.

[18] N. Papasimakis, Y. H. Fu, V. A. Fedotov, S. L. Prosvirnin, D. P. Tsai, and N. I. Zheludev. "Metamaterial with polarization and direction insensitive resonant transmission response mimicking electromagnetically induced transparency". *Appl. Phys. Lett.*, 94(21):211902, 2009.

[19] Ranjan Singh, Ibraheem A.I.Al-Naib, Martin Koch, and Weili Zhang. "Sharp fano resonances in thz metamaterials". *Optics express*, 19:6314, 2011.

[20] A. E. Miroshnichenko, S. Flach, and Y. S. Kivshar. "Fano resonances in nanoscale structures". *Rev. Mod. Phys.*, 82:2257 – 2298, 2010.

[21] A. Christ, Y. Ekinci, H. H. Solak, N. A. Gippius, S. G. Tikhodeev, and O. J. F. Martin. "Controlling the fano interference in a plasmonic lattice". *Phys. Rev. B*, 76:201405, 2007.

[22] V. A. Fedotov, M. Rose, S. L. Prosvirnin, N. Papasimakis, and N. I. Zheludev. "Sharp trapped-mode resonances in planar metamaterials with a broken structural symmetry". *Phys. Rev. Lett.*, 99(14):147401, 2007.

[23] F. Hao, Y. Sonnefraud, P. Van Dorpe, S. A. Maier, N. J. Halas, and Peter Nordlander. "Symmetry breaking in plasmonic nanocavities: Subradiant LSPR sensing and a tunable fano resonance". *Nano Lett.*, 8(11):3983–3688, 2008.

[24] Y. Sonnefraud, N. Verellen, H. Sobhani, G. A. E. Vandenbosch, V. V. Moshchalkov, P. Van Dorpe, P. Nordlander, and S. A. Maier. "Experimental realization of subradiant, superradiant, and fano resonances in ring/disk plasmonic nanocavities". *ACS Nano*, 4(3):1664 – 1670, 2010.

[25] Stefan A. Maier. "The benefits of darkness". *Nature Materials*, 8:699–700, 2009.

[26] N. Liu, T. Weiss, M. Mesch, L. Langguth, U. Eigenthaler, M. Hirscher, C. Sonnichsen, and H. Giessen. "Planar metamaterial analogue of electromagnetically induced transparency for plasmonic sensing". *Nano Lett.*, 10:1103–1107, 2010.

[27] H. Lu, X. Liu, D. Mao, and Guoxi Wang. "Plasmonic nanosensor based on fano resonance in waveguide-coupled resonators". *Optics Lett.*, 37(18):3780–3782, 2012.

[28] C. Chao and L. J. Guo. "Biochemical sensors based on polymer microrings with sharp asymmetrical resonance". *App. Phys. Lett.*, 83(8):1527–1529, 2003.

[29] B. Luk'yanchuk, N.I. Zheludev, S.A. Maier, N.J. Halas, P. Nordlander, H. Giessen, and C. Chong. "The fano resonance in plasmonic nanostructures and metamaterials". *Nature Materials*, 9:707–715, 2010.

[30] J. J. Mock, D. R. Smith, and S. Schultz. "Local refractive index dependence of plasmon resonance spectra from individual nanoparticles". *Nano Lett.*, 4(4):485–491, 2003.

[31] P. B. Johnson and R. W. Christy. "Optical constants of the noble metals". *Phys. Rev. B*, 6:4370–4378, 1972.

[32] Z. Dong, H. Liu, M. Xu, T., S.Wang, S.Zhu, and X. Zhang. "Plasmonically induced transparent magnetic resonance in a metallic metamaterial composed of asymmetric double bars". *Optics Express*, 18(17):18229 – 18234, 2010.

[33] A. Christ, T. Zentgraf, S. G. Tikhodeev, N. A. Gippius, J. Kuhl, and H. Giessen. "Controlling the interaction between localized and delocalized surface plasmon modes: Experiment and numerical calculations". *Phys. Rev. B*, 74:155435, 2006.

[34] S. Zhang, D. A. Genov, Y. Wang, M. Lui, and X. Zhang. "Plasmon induced transparency". *Phys. Rev. Lett.*, 101(4):047401, 2008.

[35] N. I. Zheludev, S. L. Prosyimin, N. Papasimakis, and V. A. Fedotov. "Lasing spacer". *Nature Photonics*, 2:351–354, 2008.

[36] E. Prodan, C. Radloff, N. J. Halas, and P. Nordlander. "A hybridization model for the plasmon response of complex nanostructures". *Science*, 302:419, 2003.

[37] S. Zhang, K. Bao, N. J. Halas, H. Xu, and P. Nordlander. "Substrate-induced fano resonances of a plasmonic nanocube: a route to increased-sensitivity localized surface plasmon resonance sensors revealed". *Nano Lett.*, 11:1657, 2011.

[38] F. Hao, P. Nordlander, Y. Sonnefraud, P. Van Dorpe, and S. A. Maier. "Tunability of subradiant dipolar and fano-type plasmon resonances in metallic ring/disk cavities: implications for nanoscale optical sensing". *ACS Nano*, 3:643 – 652, 2009.

[39] H. Yan, F. Xia, Z. Li, and P. Avouris. "Plasmonics of coupled graphene microstructures". *New J. Phys.*, 14:125001, 2012.

[40] I. A. I. Al-Naib, C. Jansen, N. Born, and M. Koch. "Polarization and angle independent terahertz metamaterials with high Q-factors". *App. Phy. Lett.*, (98):091107, 2011.

[41] H. Fujiwara. "Spectroscopic ellipsometry principles and applications". *John Wiley and Sons Ltd, England*, 2003.

[42] H.G. Tompkins and W. A. McGahan. "Spectroscopic ellipsometry and reflectometry: A user's guide". *John Wiley and Sons Ltd*, 1999.

[43] T. J. Yen, W. J. Padilla, N. Fang, D. C. Vier, D. R. Smith, J. B. Pendry, D. N. Basov,

and X. Zhang. "Terahertz magnetic response from artificial materials". *Science*, 303:1494 – 1496, 2004.

[44] T. W. H. Oates, H. Wormeester, and H. Arwin. "Characterization of plasmonic effects in thin films and metamaterials using spectroscopic ellipsometry". *Progress in Surface Science*, 86:328 – 376, 2011.

[45] E. D. Palik. "Handbook of optical constants of solids II". *Academic, New York, USA*, 1991.

[46] C. R. Simovsky. "On electromagnetic characterization and homogenization of nanostructured matematerials". *J. Opt.*, 13:013001, 2011.

[47] S. Lee, K. Lee, J. Ahn, J. Lee, M. Kim, and Y. Shin. "Highly sensitive biosensing using arrays of plasmonic au nanodisks realized by nanoimprint lithography". *ACS Nano*, 5(2):897–904, 2011.

[48] I. H. El-Sayed, X. Huang, and M. A. El-Sayed. "Surface plasmon resonance scattering and absorption of anti-egfr antibody conjugated gold nanoparticles in cancer diagnostics: Applications in oral cancer". *Nano Lett.*, 5(5):829–834, 2005.

[49] R. S. Moirangthem, M. T. Yaseen, P. Wei, J. Cheng, and Y. Chang. "Enhanced localized plasmonic detections using partially-embedded gold nanoparticles and ellipsometric measurements". *Biomed. Opt. Express*, 3(5):899–910, 2012.

[50] C. Debus and P. H. Bolivar. "Frequency selective surfaces for high sensitivity terahertz sensing". *Appl. Phys. Lett.*, 91:184102–1 – 184102–3, 2007.

[51] E. Cubukcu, S. Zhang, Y-S. Park, G. Bartal, and Xiang Zhang. "Split ring resonator sensors for infrared detection of single molecular monolayers". *Appl. Phys. Lett.*, 95:043113, 2009.

[52] X. Xu, B. Peng, D. Li, J. Zhang, L. M. Wong, Q. Zhang, S. Wang, and Q. Xiong. "Flexible visible-infrared metamaterials and their applications in highly sensitive chemical and biological sensing". *Nano Lett.*, 11:3232 – 3238, 2011.

[53] J. Homola. "Surface plasmon resonance based sensors". *Springer, Berlin*, 2006.

[54] L. J. Sherry, S. H. Chang, G. C. Schatz, R. P. Van Duyne, B. J. Wiley, and Y. N. Xia. "Localized surface plasmon resonance spectroscopy of single silver nanocubes". *Nano Lett.*, 5(10):2034–2038, 2005.

[55] P. Offermans, M. C. Schaafsma, S. R. K. Rodriguez, Y. Zhang, and M. Crego-Calama. "Universal scaling of the figure of merit of plasmonic sensors". *ASC Nano*, 5:5151 – 5157, 2011.

[56] H.-T. Chen, J. F. O'Hara, A. K. Azadi, A. J. Taylor, R. D. Averitt, D. B. Shrekenhamer, and W. J. Padilla. "Experimental demonstration of frequency-agile terahertz metamaterials". *Nat. Photonics*, 2:295 – 298, 2008.

[57] J. Carbonell, V. E. Boria, and D. Lippens. "Resonators loaded with heterostructure barriere varactos". *Microw. Opt. Technol. Lett.*, 50:474 – 479, 2008.

[58] T. H. Hand and S. A. Cummer. "Frequency tunable electromagnetic metamaterial using ferroelectric loaded split rings". *J. Appl. Phys.*, 103:066105, 2008.

[59] Q. Liu, Y. Cui, D. Gardner, X. Li, S. He, and I. I. Smalyukh. "Self-alignment of plasmonic gold nanorods in reconfigurable anisotropic fluids for tunable bulk metamaterial applications". *Nano Lett.*, 10(4):1347 – 1353, 2010.

[60] I. C. Khoo, D. H. Werner, X. Liang, A. Diaz, and B. Weiner. "Nanosphere dispersed liquid crystals for tunable negative-zero-positive index of refraction in the optical and terahertz regimes". *Optics Lett.*, 31(17):2592 – 2594, 2006.

[61] M. Kleman and O. D. Lavrentovich. "Soft matter physics: An introduction". *Springer, New York*, Chapter 4:42 – 134, 2003.

[62] D. H. Werner, D.-H. Kwon, I.-C. Khoo, A. V. Kildishev, and V. M. Shalaev. "Liquid crystal clad near-infrared metamaterials with tunable negative-zero-positive refractive indices". *Optics Express*, 15:3342 – 3347, 2007.

[63] X. Wang, D.-H. Kwon, D. H. Werner, I.-C. Khoo, A. V. Kildishev, and V. M. Shalaev. "Tunable optical negative-index metamaterials employing anisotropic liquid crystals". *Appl. Phys. Lett.*, 91:143122, 2007.

[64] F. Zhang, L. Kang, Q. Zhao, J. Zhou, X. Zhao, and Didier Lippens. "Magnetically tunable left handed metamaterials by liquid crystal orientation". *Optics Express*, 17:4360–4366, 2009.

[65] F. Zhang, Q. Zhao, L. Kang, D. P. Gaillot, X. Zhao, J. Zhou, and D. Lippens. "Magnetic control of negative permeability metamaterials based on liquid crystals". *Appl. Phys. Lett.*, 92:193104, 2008.

[66] R. Pratibha, K. Park, I. I. Smalyukh, and W. Park. "Tunable optical metamaterial based on liquid crystal-gold nanosphere composite". *Optics Express*, 17:19459–19469, 2009.

[67] A. Minovich, D. N. Neshev, D. A. Powell, I. V. Shadrivov, and Y. S. Kivshar. "Tunable fishnet metamaterials infiltrated by liquid crystals". *Appl. Phys. Lett.*, 96: 193103, 2010.

[68] J. Li, Y. Ma, Y. Gu, I. Khoo, and Qihuang Gong. "Large spectral tunability of narrow geometric resonances of periodic arrays of metallic nanoparticles in a nematic liquid crystal". *Appl. Phys. Lett.*, (98):213101, 2011.

[69] J. Li, S. T. Wu, S. Brugioni, R. Meucci, and S. Faetti. "Infrared refractive indices of liquid crystals". *J. Appl. Phys.*, 97:073501, 2005.

[70] K. R. Amundson and M. Srinivasarao. "Liquid-crystal-anchoring transitions at surfaces created by polymerization-induced phase separation". *Phys. Rev. E*, 58(2): 1211, 1998.

[71] G. P. Bryan-Brown, E. L. Wood, and I. C. Sage. "Weak surface anchoring of liquid crystals". *Nature*, 399:338–340, 1999.

[72] K. R. Amundson. "Imprinting of nematic order at surfaces created by polymerization-induced phase separation". *Phys. Rev. E*, 58:3273 – 3279, 1998.

[73] Y. Arakawa, S. Nakajima, S. Kang, M. Shigeta, G. Konishi, and Junji Watanabe. "Design of an extremely high birefringence nematic liquid crystal based on a dinaphthyl-diacetylene mesogen". *J. Mater. Chem.*, 22:13908 – 13910, 2012.

[74] L. Wang, X. Lin, X. Liang, J. Wu, W. Hu, Z. Zheng, B. Jin, Y. Qin, and Yan qing Lu. "Large birefringence liquid crystal material in terahertz range". *Opt. Mat. Exp.*, 2: 1314–1319, 2012.